

Laminin-coated electronic scaffolds with vascular topography for tracking and promoting the migration of brain cells after injury

Received: 8 November 2022

Accepted: 30 August 2023

Published online: 9 October 2023

 Check for updates

Xiao Yang   ^{1,2,10}, Yue Qi ^{1,6,10}, Chonghe Wang ^{3,7}, Theodore J. Zwang  ^{1,8}, Nicholas J. Rommelfanger  ⁴, Guosong Hong  ⁵  & Charles M. Lieber  ^{1,3,9} 

In the adult brain, neural stem cells are largely restricted into spatially discrete neurogenic niches, and hence areas of neuron loss during neurodegenerative disease or following a stroke or traumatic brain injury do not typically repopulate spontaneously. Moreover, understanding neural activity accompanying the neural repair process is hindered by a lack of minimally invasive devices for the chronic measurement of the electrophysiological dynamics in damaged brain tissue. Here we show that 32 individually addressable platinum microelectrodes integrated into laminin-coated branched polymer scaffolds stereotactically injected to span a hydrogel-filled cortical lesion and deeper regions in the brains of mice promote neural regeneration while allowing for the tracking of migrating host brain cells into the lesion. Chronic measurements of single-unit activity and neural-circuit analyses revealed the establishment of spiking activity in new neurons in the lesion and their functional connections with neurons deeper in the brain. Electronic implants mimicking the topographical and surface properties of brain vasculature may aid the stimulation and tracking of neural-circuit restoration following injury.

In the case of brain damage such as a stroke, where a large cell population undergo cell death, the recruitment of neural stem cells to restore lost functions is important¹. The repair process in response to brain cell loss involves neural stem cells that self-renew, differentiate and develop under specific biophysical and biochemical cues^{2–4}. Transplantation of exogenous stem cells has the potential to treat brain injuries⁵; however, exogenous stem cells can have high rejection rates

owing to immune and inflammatory responses⁶. On the other hand, endogenous neural stem cells are not limited by the foreign-body response, and therefore represent a promising therapeutic approach. However, endogenous neural stem cells in the adult brain are largely confined in two spatially discrete neurogenic niches. In the absence of a structural support, it is challenging to repopulate a lesion cavity and to regenerate functional brain tissue. It has recently been shown

¹Department of Chemistry and Chemical Biology, Harvard University, Cambridge, MA, USA. ²Department of Psychiatry and Behavioral Sciences and Department of Chemistry, Stanford University, Stanford, CA, USA. ³John A. Paulson School of Engineering and Applied Sciences, Harvard University, Cambridge, MA, USA. ⁴Department of Applied Physics, Stanford University, Stanford, CA, USA. ⁵Department of Materials Science and Engineering, Stanford University, Stanford, CA, USA. ⁶Present address: Beijing Graphene Institute, Beijing, China. ⁷Present address: Department of Mechanical Engineering, Massachusetts Institute of Technology, Cambridge, MA, USA. ⁸Present address: Department of Neurology, MassGeneral Institute for Neurodegenerative Disease, Massachusetts General Hospital, Charlestown, MA, USA. ⁹Present address: Lieber Research Group, Lexington, MA, USA.

¹⁰These authors contributed equally: Xiao Yang, Yue Qi.  e-mail: xiaoy1@stanford.edu; guosongh@stanford.edu; liebercharlesm@gmail.com

that biomaterials can provide structural support and promote the migration of host cells into a lesion site for repair and recovery^{4,7–9}. Despite these important discoveries, it remains unclear whether it is possible to provide *in vivo* time-lapse evidence within the damaged site and surrounding tissue, and to show that the infiltrated cells can rebuild neural tissue with functional neural circuits. These open questions are crucial for understanding the spatiotemporal dynamics of endogenous neural regeneration and repair, and thus are of great importance when seeking out new directions for future therapies.

Flexible bioelectronic devices have been developed with the capability to probe and modulate neural activity with high spatiotemporal resolution. Moreover, they can have long-term stability, low invasiveness and, in some cases, seamless tissue-electronics interfaces^{10–13}. Notably, bioelectronics can function not only as chronic recording and stimulation interfaces for *in vitro*^{14–16} and *in vivo* nervous systems^{17–21}, but also as bioactive scaffolds used for *in vitro* cell culture¹⁴ and impact cell migration *in vivo*¹⁷. In this Article, we leveraged the insights gained from the endogenous self-repair process to design and develop a multimodal three-dimensional (3D) vasculature-like electronic scaffold for simultaneously inducing and monitoring migration and functional wiring of neural circuits in mice following a brain lesion.

Results

First, we asked whether it was possible to rationally design an electronic scaffold to promote brain regeneration and simultaneously monitor such a process. The design of our electronic scaffold is inspired by recent studies that show newborn neurons derived from the subventricular zone (SVZ), one of the two neurogenic niches in the adult mammalian brain, exhibit vasculature-guided neuronal migration via laminin-mediated perivascular ligand-receptor interaction towards the olfactory bulb (OB) under normal physiological conditions^{22,23} (Fig. 1a), or towards the affected area in the post-stroke brain²⁴. Thus, we designed a vasculature-like electronic scaffold (VasES) by tailoring its topographical features and surface properties to adopt the properties of vasculature to facilitate the migration of newborn neurons (Fig. 1b). Specifically, the topographical features of the electronic scaffold were designed to emulate the fractal organization and branched structure of blood vessels at comparable dimensions²⁵ (Fig. 1c). The ca. 4-μm-wide interconnects recapitulate the size of arteries and veins in the brain, and the ca. 1.5-μm-wide branches are comparable to the capillaries (Supplementary Fig. 1). Notably, these feature sizes are also consistent with those shown to provide optimal guidance cues to direct neurite outgrowth and neural cell migration²⁶. Moreover, given that the interactions between the biological microenvironment and materials are strongly influenced by the materials' surface properties^{7,8}, including studies of surface-modified silicon probes to reduce glial scarring²⁷, we endowed the surface of the electronic scaffold with vasculature-mimicking properties by functionalizing it with laminin, a major component of the basement membrane of blood vessels²⁸. Specifically, the polymer surface of the electronic scaffold was uniformly functionalized with laminin through covalent coupling (Supplementary Fig. 2). Such covalent coupling is stable without loss of fluorescence or surface coverage for at least 2 weeks (Supplementary Fig. 2c–g). We incorporated 32 individually addressable 20-μm-diameter platinum electrodes into the scaffold structure to enable single-unit electrophysiological recording (Supplementary Table 1 and Methods). This rationally designed 3D electronic scaffold presenting tailored biophysical and biochemical cues was termed VasES.

To evaluate the regeneration efficacy induced by our rationally designed VasES in an unambiguous manner, we designed and implemented a brain resection mouse model (Fig. 1a,b, Extended Data Fig. 1 and Methods). As shown in Fig. 1a, superficial layers of the cerebral cortex were resected from the mouse brain. Matrigel matrix^{14,28}, a natural extracellular matrix-based hydrogel, was injected into the

resection cavity. The VasES was stereotactically implanted through the Matrigel-filled resection, the remaining cortex and the neurogenic niche SVZ to allow the built-in sensors spanning the resection and the host brain tissue (Fig. 1b and Supplementary Fig. 3a). The abundance of cells that infiltrated into the brain resection along the VasES was used to assess the efficacy of neural regeneration.

As shown in the 3D fluorescence images at the resection boundary (Fig. 1d and Supplementary Fig. 3b), VasES (red) shares similar topographical features and dimensions with tomato lectin (TL)-labelled vasculature (magenta) of the mouse brain. Close-up images of the fluorescently labelled polymer material and vasculature-like surface functionalization of VasES (Fig. 1e,f) demonstrate a complete coverage and uniform coating of the laminin functionalization on the surface of VasES. Overlay visualization and quantitative co-localization analysis demonstrates a strong correlation between the fluorescently labelled polymer and surface-bound fluorescently tagged laminin (Supplementary Fig. 3c,d), highlighting the complete coverage and uniform coating of laminin functionalization in a quantitative manner.

We asked whether the rationally designed VasES with tailored biophysical and biochemical functionalities can promote the migration of newborn neurons. To this end, we first examined the performance of VasES in guiding the migration of SVZ newborn neurons in the native tissue and compared it with its structurally and biochemically unmodified control probes and biochemically unmodified VasES (without laminin). Microtubule-associated protein doublecortin (DCX) is a stage-specific marker transiently expressed in migrating immature neurons, and has been widely used to study neurogenesis and neuronal migration²³. Fluorescence images and quantitative analyses showed the abundance of DCX⁺ newborn neurons were increased two fold for the VasES without laminin compared with the control probes and a further 2.2-fold increase for the laminin-functionalized VasES relative to unmodified VasES (Extended Data Fig. 2). These data show that both the branched structural topography and laminin functionalization contribute in a statistically significant manner for recruiting and directing the migration of newborn neurons with the VasES probes. Chronic electrophysiological recordings showed significantly higher single-unit spike signal-to-noise ratios recorded by VasES compared with control probes at 1–2 weeks post-implantation (Extended Data Fig. 3). Together, these immunohistochemistry and electrophysiology studies demonstrated that VasES outperforms its unmodified counterpart in recruiting newborn neurons to the vicinity of the probes, and thus VasES was used for further studies in the cortical resection model as detailed below. Notably, finite-element simulations (Supplementary Table 1 and Supplementary Note 1) reveal that the effective bending stiffness of VasES is <3% greater than that of the control probes. This implies that the observed differences are unlikely due to the small differences in mechanical properties.

Given the pro-regenerative characteristic of VasES in the native tissue, we asked whether it can direct brain regeneration in the cortical resection. First, to establish the baseline, we assessed whether newborn neurons naturally migrate into the Matrigel-filled resection without VasES implantation by performing a control resection surgery. Histological assessment of newborn neurons at 1 week post-surgery (Fig. 2a and Extended Data Fig. 4a) demonstrated that no newborn neurons infiltrated into the resection, although there are some newborn neurons at the resection boundary due to the endogenous regeneration mechanism^{29,30}. Then, we implanted the VasES through the resection, remaining cortex and SVZ. Fluorescence imaging shows that newborn neurons migrate from SVZ along the VasES into the resection to a distance as far as ca. 800 μm after 1 week (Fig. 2b and Extended Data Fig. 4b). Higher-resolution imaging further demonstrates that these migrating newborn neurons formed elongated chain-like cell aggregates, and the orientation of these chains corresponds to the direction of migration (Fig. 2c and Extended Data Fig. 4c–e). Notably, the leading processes of these newborn neurons were closely

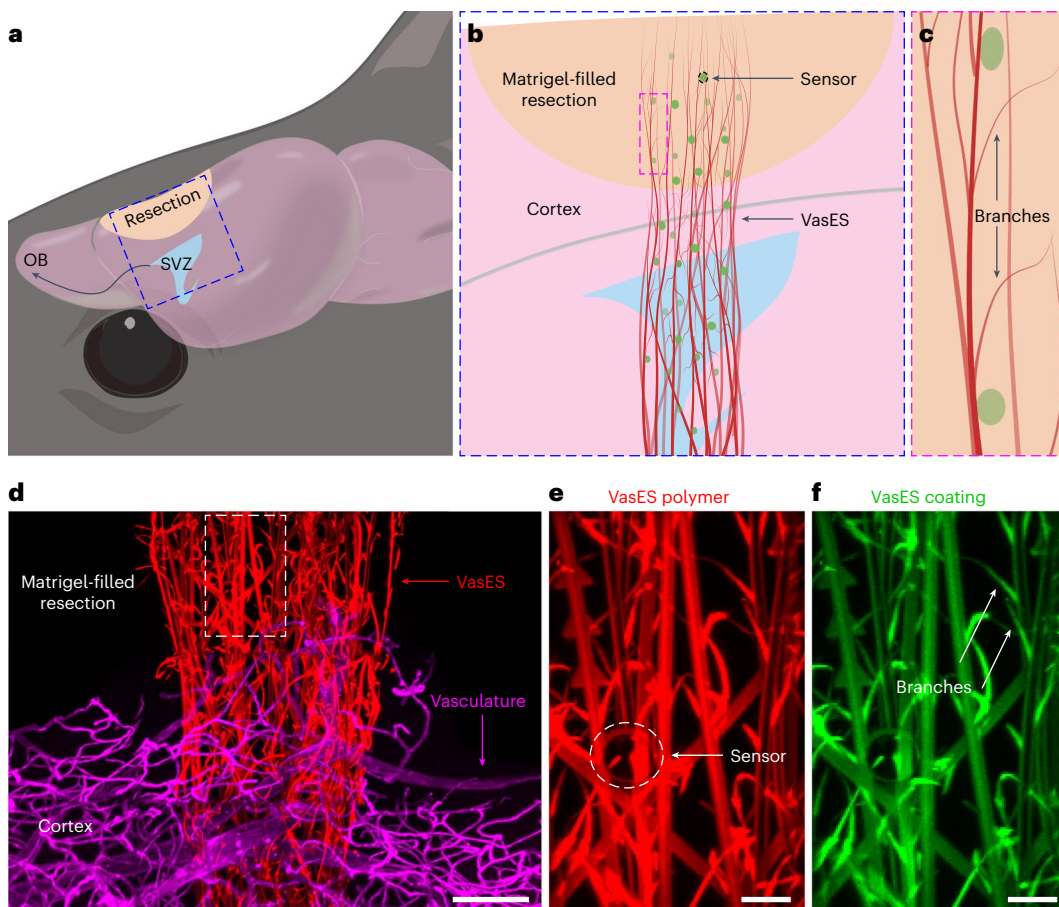


Fig. 1 | Experimental design for vasculature-like electronics as migratory scaffolds for brain regeneration. **a**, Schematic of a mouse brain that has undergone cortical resection. The arrow indicates neural progenitor cells from SVZ migrate along the rostral migratory stream to the OB. **b**, Close-up schematic of the region highlighted by the blue dashed box in **a**, showing VasES bridging the neurogenic niche SVZ and cortical resection. VasES, sensors, resection, tissue and SVZ are in red, green, yellow, pink and blue, respectively. **c**, Close-up schematic of the region highlighted by the magenta dashed box in **b**, showing

vasculature-mimicking topography of VasES. **d**, Fluorescence microscope image of VasES (red) and tomato lectin-labelled blood vessels (magenta) at the resection boundary, demonstrating the vasculature-mimicking topographical property of VasES. Scale bar, 150 μ m. **e,f**, Close-up fluorescence microscope images of Lissamine RhBn-labelled polymer (**e**) and HiLyte 488-labelled laminin functionalization (**f**) in the white dashed box in **d**, highlighting the vasculature-mimicking surface property through uniform and complete laminin functionalization. Scale bars, 20 μ m.

associated and aligned with VasES elements. To quantitatively analyse the extent of newborn neuron association with VasES, we assessed the abundance of DCX⁺ newborn neurons as a function of the distance from VasES in the cortical resection. As shown in Fig. 2d, substantial DCX⁺ newborn neurons are in close proximity to VasES. As summarized in Fig. 2e, normalized DCX fluorescence intensity near VasES is statistically significantly higher than far from VasES and Matrigel control samples without VasES implantation. Control experiments show that a small level (ten fold less) of DCX⁺ cells migrate on VasES into the resection even when it is not implanted into the SVZ (Extended Data Fig. 4). These results highlight that VasES functions as a structural and bioactive 3D scaffold that promotes neuronal cell migration and tissue regeneration.

Moreover, given the important role of astrocytes in facilitating synapse formation and neuron physiological maturation, as well as regulating the functional synaptic integration of adult-born neurons³¹, we asked whether astrocytes also migrate into the resection in addition to newborn neurons. Histology studies at 1 week post-implantation show that astrocytes migrate along the VasES into the resection, with their projections aligned with VasES structures (Extended Data Fig. 5). To examine the infiltration of endothelial cells and microglia, we retro-orbitally injected *Lycopersicon esculentum* TL DyLight 649 into VasES-implanted mice^{32,33} (Methods). This data

(Extended Data Fig. 6a,b) demonstrates that TL⁺ endothelial cells and microglia were present in the cortical resection at both 1 and 2 weeks post-implantation.

Given the diverse cell types infiltrated into the resection, we further asked whether the migrating newborn neurons subsequently develop into mature neurons at a later stage. To this end, we examined the expression of mature neuron marker NeuN at 4 weeks post-implantation^{23,30}. Representative fluorescence images (Extended Data Fig. 7a–c) show the association of NeuN⁺ neurons with VasES in the resection, indicating the maturation, at least partly, of newborn neurons into mature neurons. Quantitative analysis of normalized NeuN fluorescence intensity on multiple independent samples shows that NeuN⁺ neurons are concentrated near the VasES as opposed to baseline (Extended Data Fig. 7). As shown in Extended Data Fig. 6c,d, neurofilaments were also observed associating with the VasES in the cortical resection at 4 weeks and 3 months post-implantation, indicating the infiltration of axons. Together, these data showing the infiltration of newborn neurons, neuronal nuclei and axons, astrocytes, microglia and endothelial cells suggest the potential of VasES in promoting tissue formation by inducing the migration and repopulation of diverse cell types that are critical for reconstructing tissue architecture and cellular composition. In the future, further studies of the cell composition in the VasES-implanted cortical resection, such as the

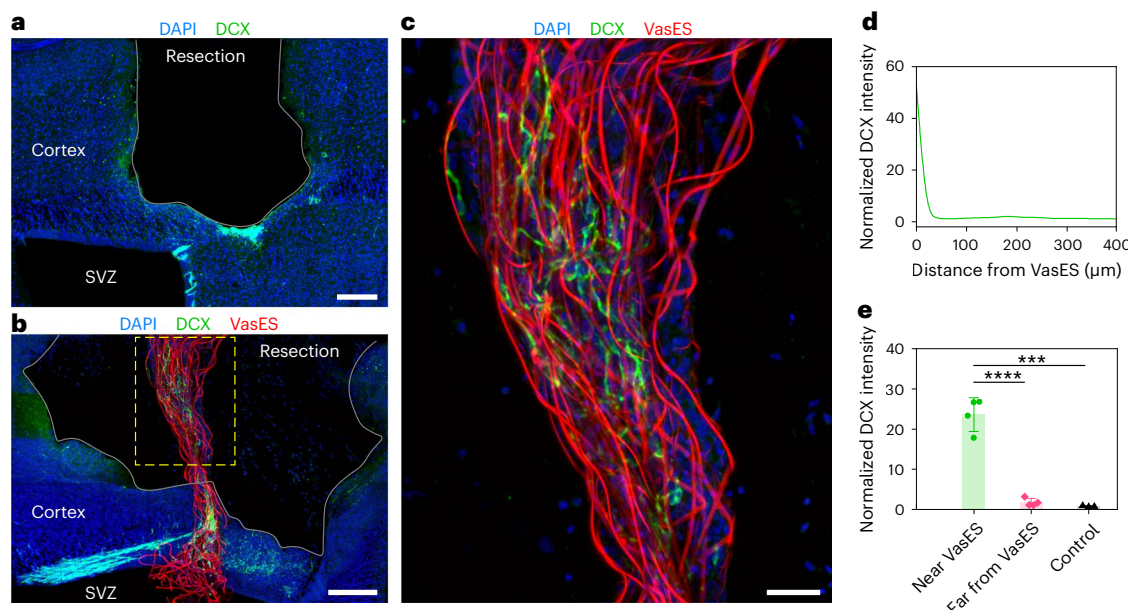


Fig. 2 | Migration of newborn neurons from SVZ into the cortical resection along the VasES. **a**, Fluorescence image of control resection without implantation shows no newborn neurons infiltrated into the resection at 1 week post-implantation. **b**, Fluorescence image shows substantial newborn neurons migrating along the VasES into the brain resection to a distance of ca. 800 μm as soon as 1 week post-implantation. The grey curves in **a** and **b** delineate the resection boundaries. Scale bars in **a** and **b**, 200 μm . **c**, Close-up image of the volume highlighted by the yellow dashed box in **b**, showing the leading processes of newborn neurons are aligned with VasES elements. Scale bar, 50 μm . **d**, DCX

fluorescence intensity profile as a function of the distance from VasES corresponding to **c**, demonstrating concentrated newborn neurons near VasES as opposed to baseline. The fluorescence intensity was normalized to the baseline value away from VasES to obtain the relative signal, as detailed in Supplementary Note 3. **e**, Quantitative analysis of normalized DCX fluorescence intensity at 0–60 μm from VasES (near VasES), 300–360 μm from VasES (far from VasES) and without VasES implantation (control) at 1 week post-surgery. $N = 4$ independent samples for near VasES and far from VasES, and $N = 3$ independent control samples. *** $P < 1 \times 10^{-4}$, *** $P < 1 \times 10^{-3}$, two-tailed t -test. Error bars reflect ± 1 s.d.

examination of oligodendrocytes and cortical layer markers, may also be interesting to pursue.

Inspired by these exciting histology results, which show the migration of newborn neurons into the resection, we asked whether these neurons are functionally active and form and/or integrate into neural circuits. Understanding these fundamental questions is critical given the implications of rebuilding function circuits to post-injury recovery, but has been elusive so far due to the lack of access to single-neuron electrophysiology in a minimally invasive and chronic manner. To this end, we implanted the VasES such that its built-in electrodes are distributed across the cortical resection, remaining cortex and SVZ (Fig. 3a), which allows us to study the neuronal activity chronically across these brain regions. We followed the electrophysiology for a month post-implantation, and the *in situ* 3D neural interfaces were imaged at the endpoint of the measurements to spatially register the electrodes with respect to the resection and host brain regions according to the channel-indexing barcodes (Supplementary Fig. 4). The results highlight several key points. First, at 12 h post-implantation, action potential spikes were recorded in the host brain tissue but not in the resection (Fig. 3a,I) due to the complete removal of tissue in the resection. Second, new spikes appeared in the resection starting from 1 week (Fig. 3a,II and Supplementary Fig. 5a), suggesting that some of the migrating newborn neurons are spontaneously active. As shown in Fig. 3b and Supplementary Fig. 5b, we carried out principal component analysis (PCA) to identify individual neurons. PCA-clustered single units from representative channels in the cortical resection (Ch 23 and Ch 26) showed no single-unit spikes at 12 h, but started to record new single units at 1 week. On the other hand, the electrodes distributed across different regions in the host brain tissue, as represented by Ch 1, Ch 2 and Ch 17 (Fig. 3b and Supplementary Fig. 5b), recorded single units as soon as 12 h after surgery. In addition, the interfacial electrode impedance values were relatively constant at $0.5 \pm 0.1 \text{ M}\Omega$ (mean \pm s.d.)

over the course of our recording measurements (Supplementary Fig. 6), showing that any changes are not due to spurious electrochemical effects. Together, these time-lapse electrophysiology studies and analyses suggest that functionally active newborn neurons infiltrated into the cortical resection from about 1 week post-implantation.

We carried out comprehensive analyses on the electrodes distributed across the resection, and host cortical and subcortical regions on this mouse (mouse 1) and two additional mice (mouse 2 and mouse 3) across eight timepoints over a month. These data and analyses (summarized in Fig. 3c and detailed in Supplementary Figs. 5 and 7) show a consistent trend of new active neurons emerging in the resection at about 1–2 week(s), while many electrodes in the cortical and subcortical regions of the host brain tissue started to record signals within 12–24 h. We also note that some neural spike signals in the resection are lost with time (Fig. 3c and Supplementary Fig. 7b), although this is consistent with the ongoing dynamic changes occurring within the resection. Overall, these data and analyses from multiple independent animals show the migration of newborn neurons into the resection and their subsequent spontaneous spiking, which represents a dramatic form of neural plasticity exploited by bioscaffolds³⁴. We note that the electrophysiological data, in conjunction with the histological data, suggest that functionally active newborn neurons primarily contribute to the migration into the cortical resection along the VasES. Nevertheless, these data cannot completely rule out the possibility that some mature neurons also migrate to the resection site.

The observation of functionally active newborn neurons in the resection led us to ask whether these newborn neurons form synaptic connections and neural circuits with each other and with the host brain³⁵. The question about active circuits is critical in evaluating whether regeneration produces recovery in which the new cells develop into neurons with the functional connections of the neurons they replace³⁶. Specifically, we wanted to gain insight into whether these

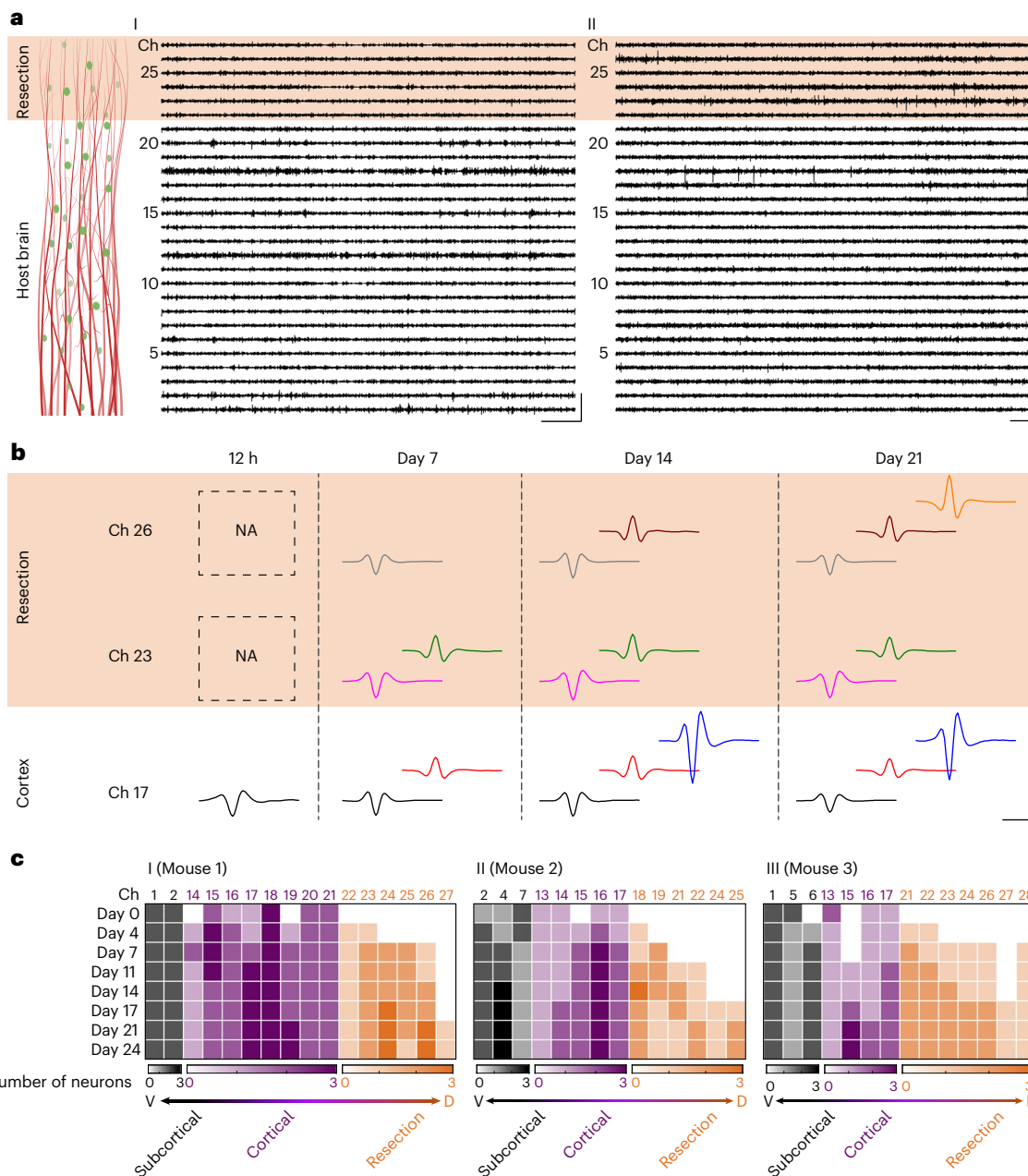


Fig. 3 | Emergence of functionally active newborn neurons in the cortical resection. **a**, Representative 27-channel single-unit spike traces of mouse 1 at 12 h (I) and 21 days (II) post-implantation. The x and y axes represent recording time and voltage, respectively. The left-most inset shows the schematic of VasES implantation with respect to cortical resection and host brain tissue as revealed by electrode registration detailed in Supplementary Fig. 4. Scale bars, 50 ms (lateral) and 100 μ V (vertical). **b**, Time evolution of spikes of PCA-clustered single units from three representative channels in the resection and host cortex over 3 weeks post-injection. Each distinct colour in the sorted spikes represents a unique identified neuron. ‘NA’ denotes ‘not available’, indicating that no single-

unit spikes were detected at this time point. The scale bars for 12 h, day 7, day 14 and day 21 are 1 ms (lateral) and 50 μ V (vertical) and are shown once on the right. **c**, Heat maps of the number of distinct neurons recorded per electrode in the subcortical (black), cortical (purple) and resection (orange) regions as a function of the time post-injection. I is from mouse 1, and II and III are from two additional independent mice, mouse 2 and mouse 3, with raw traces and detailed analyses in Supplementary Figs. 5 and 7. ‘V’ and ‘D’ represent ventral and dorsal, respectively. These data highlight the reproducibility of emergence of functionally active newborn neurons in the resection.

newborn neurons migrated into the resection are involved in remote or local neural circuits, including interregional connections between the resection and the remaining host cortex and intraregional connections within the resection (Fig. 4a); and moreover, how the wiring diagram changes dynamically as a function of time. To this end, we analysed putative circuit interactions at different timepoints post-implantation by calculating cross-correlation coefficients between pairs of neurons (Supplementary Note 2). Time-lapse

cross-correlograms (CCGs) from 0 to 21 days of a representative pair of neurons, that is, the magenta neuron recorded by Ch 23 in the resection and the blue neuron recorded by Ch 17 in the remaining host cortex (Fig. 4b(I)), is shown in Fig. 4b(I) and highlights several points. First, within 11 days after implantation, these two neurons have not both emerged, rendering no CCG to be calculated. Second, the first timepoint that both spontaneously active neurons emerged is day 14, while the relatively flat CCG without prominent peaks or troughs indicates there

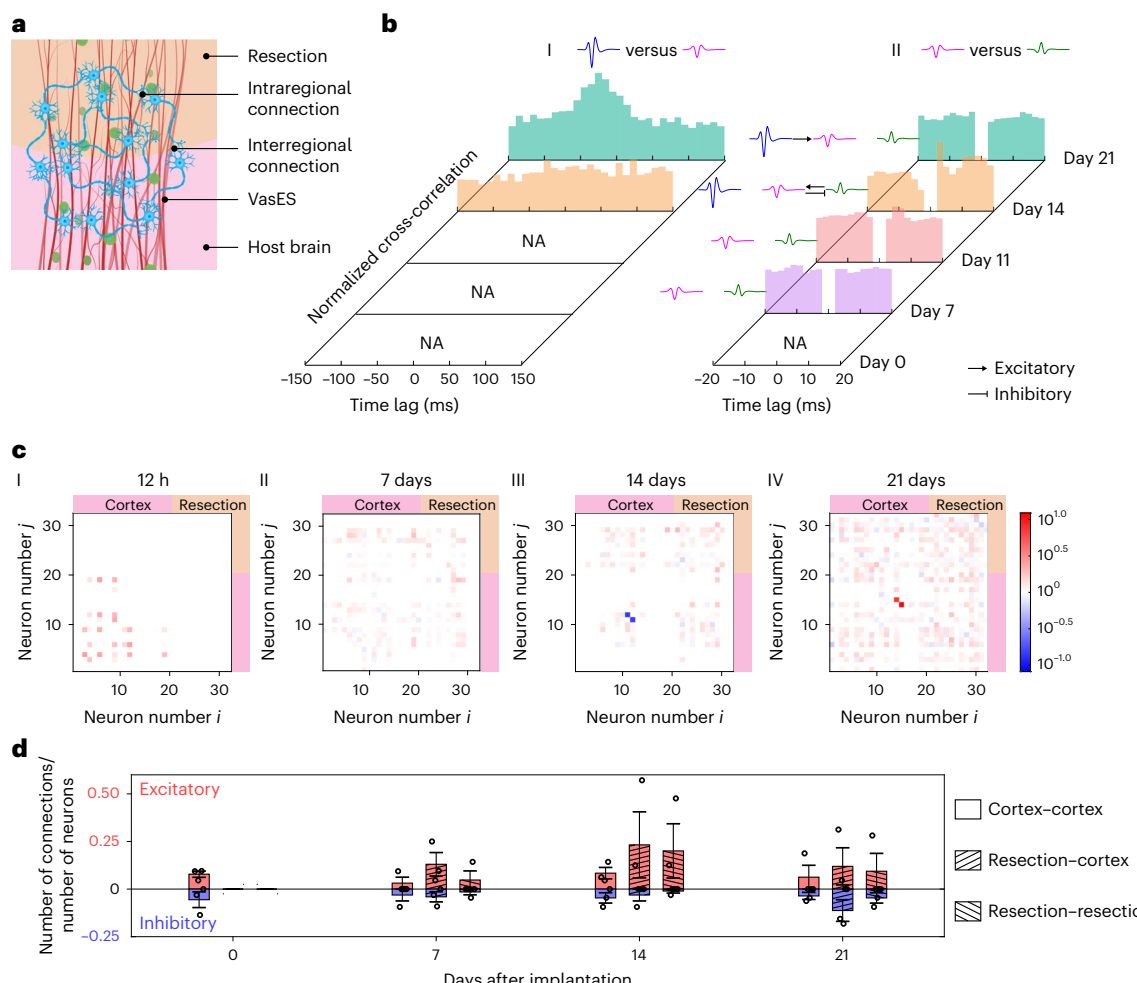


Fig. 4 | Neurons migrated into the cortical resection are involved in circuit rewiring. **a**, Intra- and interregional circuit rewiring diagram. VasES, sensors, resection, tissue and neurons are in red, green, yellow, pink and blue, respectively. **b**, Time-lapse interregional circuit wiring dynamics between the blue neuron recorded by Ch 17 in the cortex and the magenta neuron recorded by Ch 23 in the resection (I), and intraregional circuit wiring dynamics between the magenta and green neurons recorded by Ch 23 in the resection (II). **c**, Connectivity matrices of cross-correlation IS between pairs of neurons

across cortical resection and remaining host cortex as a function of time post-implantation. Each entry represents the IS from neuron number *i* to neuron number *j*. IS > 1 indicates putative excitatory interaction (red), IS < 1 indicates putative inhibitory interaction (blue) and IS of ca. 1 indicates no interaction (ca. white). **d**, Time-lapse dynamics of the number of putative excitatory connections (red) and inhibitory connections (blue) determined by IS. Error bars reflect ± 1 s.e.m. ($N = 3$ independent samples).

is no observable interaction between them. Third, on day 21, the two neurons produce a CCG featuring a broad peak with full width at half maximum of approximately 70 ms. This temporally dispersed CCG peak indicates putative excitatory functional connections categorized as a broad-type interaction^{37,38} between the neurons in the resection and the remaining host cortex. It is likely that a common input derived from cell assemblies that are spatially distributed between the coupled regions, that is, the resection and remaining cortex, but function synchronously as one unit.

In addition, the two neurons recorded by Ch 23 in the resection (the magenta and green neurons in Fig. 3b) produce CCGs with dynamic short-type interactions (Fig. 4b(II)), where the temporal characteristics are typical of putative monosynaptic interactions. Interestingly, the timepoints corresponding to the formation and dissociation dynamics of circuit interactions of these two neuron pairs are correlated, that is, the establishment of broad-type interregional interaction from days 14 to 21 of neuron pair I is accompanied by the dissociation of inhibitory and excitatory short-type intraregional interactions of neuron pair II. Notably, these characteristic short-type and broad-type interactions are not present in any of the other CCGs

of other possible neuron pairs recorded by Ch 17 and Ch 23 (Supplementary Fig. 8), demonstrating the validity of our single-unit spike sorting and cross-correlation analysis. Together, these observations suggest that the newborn neurons migrated into the resection are involved in the dynamic formation and dissociation of putative remote and local connections. Moreover, it also suggests that individual neurons were interconnected through monosynaptic and polysynaptic pathways that provides evidence of network interactions, and highlights the synaptic plasticity of the neural circuits surrounding the pro-regenerative VasES.

These findings showing circuit connectivity from representative pairs of neurons prompted us to perform comprehensive cross-correlation analyses of all possible combinations across the 32 neurons recorded in the host cortex and the resection to evaluate the spatiotemporal dynamics of putative circuit interactions. Interaction strength (IS), a metric that quantifies the strength of short-type interaction and circuit connectivity³⁹, was extracted from CCGs to produce time-lapse functional connectivity matrices across all the neuron pairs recorded in the resection and remaining cortex (Fig. 4c). As newborn neurons infiltrated into the resection after brain resection and VasES

implantation, we found IS values that indicate excitatory interactions (IS >1; red) and inhibitory interactions (IS <1; blue). We derived the number of putative excitatory and inhibitory connections from these IS values, which suggests an overall increase in the number of putative connections as a function of time (Fig. 4d). Together, the repopulation of brain resection with endogenous newborn neurons and their dynamic rewiring represent a dramatic form of neural plasticity⁴⁰ induced and promoted by the VasES. Preliminary motor behaviour studies using the rotarod test⁴¹ suggest that mice with VasES implantation following cortical resection exhibited faster motor recovery than those without VasES implantation (Supplementary Fig. 9), although future research involving multiple sensorimotor tests and other complementary measurements will be necessary to further understand these promising changes.

Notably, the capability of VasES to measure chronic time-lapse connectome at single-neuron resolution across multiple brain regions with minimal perturbation to the tissue is distinct from other connectome approaches using serial electron microscopy⁴², super-resolution optical microscopy⁴³ and viral vector tracing⁴⁴ where time-lapse information is absent and sample preparation is destructive, as well as functional magnetic resonance imaging method⁴⁵ where the spatiotemporal resolution is orders of magnitude lower than the single-neuron precision of our approach. Our technology allows for both supporting and monitoring functional tissue regeneration and circuit rewiring continuously in live animals over a month and potentially even longer given that prior studies using unmodified electronic probes with similar device structure have shown seamless integration and stable brain recording for over a year^{17,46}. That said, it will be interesting to further evaluate the long-term stability of surface-modified VasES probes in the future. These unique capabilities could allow tracking functional recovery in a range of pathological conditions such as traumatic brain injury and stroke over months of therapy that are typical for rehabilitation⁴⁷.

Discussion

The topographically tailored and biochemically functionalized 3D electronic scaffold VasES promotes the migration and functional integration of endogenous newborn neurons into resected brain tissue for brain regeneration. Our demonstrations of VasES with built-in sensors across the resected and host brain tissues present substantial future opportunities for active bioelectronic scaffolds in treating brain diseases while simultaneously monitoring such recovery during treatment. Moreover, this study suggests that leveraging the intrinsic neurogenesis in combination with bioelectronics can be a promising approach for the functional restoration of damaged neural circuits following injury to the central nervous system.

Methods

Design and fabrication of VasES

The design and structural parameters of VasES are distinct from previous reports^{48,49}, although the overall fabrication approach is similar to our previous reports^{48,49}. The topographical design patterns of the VasES and control probes are shown in Supplementary Fig. 1. Rational design of the distribution of built-in electrodes allows implantation of electrodes spanning desired regions when coupled with a controlled stereotaxic injection method as described in ‘In vivo mouse survival surgery’ section. Barcodes based on a unique combination of triangles and circles associated with electrodes (Supplementary Fig. 4) were introduced for indexing the recording electrodes. Here, we focus on 32-channel VasES, but note that higher channel numbers can be achieved by using higher-resolution fabrication^{50,51}.

The key fabrication steps for VasES probes are as follows: (1) a 100-nm-thick Ni sacrificial layer was thermally evaporated (Sharon Vacuum Co.) onto a 3 inch Si wafer (n-type 0.005 Ω cm, 600 nm thermal oxide; NOVA Electronic Materials), which was pre-cleaned with oxygen plasma (100 W, 5 min; AST Products). (2) The Si wafer was

cleaned with oxygen plasma again (100 W, 2 min) immediately before the next step. (3) The Si wafer was spin-coated with lift-off resist LOR 3A (MicroChem) at 4,000 rpm and baked at 180 °C for 3 min. Positive photoresist (Shipley 1805, Microposit, Dow Chemical Company) was spin-coated on the Si wafer at 4,000 rpm and baked at 115 °C for 5 min. The positive photoresist was patterned by photolithography (PL) with a mask aligner (SUSS MJB4 mask aligner, SUSS MicroTec) and developed (MF-CD-26, Microposit, Dow Chemical Company) for 90 s. (4) After a flood exposure of the whole Si wafer, a 3-nm-thick Cr layer and a 100-nm-thick Au layer were sequentially deposited by electron-beam evaporation (Denton Vacuum), followed by a lift-off step (MF-CD-26) for the Au input/output (I/O) pads. (5) Steps 3 and 4 were repeated for PL patterning and deposition of bottom Pt electrodes (5-nm-thick Cr and 80-nm-thick Pt). (6) Negative photoresist SU-8 2000.5 (MicroChem) was diluted in cyclopentanone (Sigma-Aldrich) at a 4:1 ratio, spin-coated on the Si wafer at 4,000 rpm, pre-baked sequentially at 65 °C for 1 min and 95 °C for 4 min, and patterned by PL. After PL exposure, the Si wafer was post-baked sequentially at 65 °C for 3 min and 95 °C for 3 min. (7) The negative photoresist was developed (SU-8 Developer, MicroChem) for 2 min, rinsed with isopropanol, dried with N₂ and hard baked at 180 °C for 1 h. (8) Negative photoresist SU-8 2000.5 was mixed with Lissamine rhodamine B ethylenediamine (RhBen; ca. 10 µg ml⁻¹; Thermo Fisher Scientific) and placed in the dark at room temperature for 3 days. The primary amine groups of RhBen covalently react with the epoxide groups of SU-8 to afford stable fluorescence labelling¹⁷. The SU-8/RhBen solution was centrifuged (Thermo Fisher Scientific) at 10,000 rpm for 3 min immediately before use to eliminate any possible undissolved RhBen. PL using the supernatant of SU-8/RhBen solution was performed by repeating steps 6 and 7 at 3,000 rpm to pattern the bottom SU-8 layer. (9) Steps 3 and 4 were repeated for PL patterning of the Au interconnect layer. (10) Step 8 was repeated for PL patterning of the top SU-8 layer as the encapsulation and insulating layer of the Au interconnect lines. The Si wafer was hard baked at 190–195 °C for 1 h to allow interdiffusion of the bottom and top SU-8 layers. (11) Steps 3 and 4 were repeated for PL patterning and deposition of top Pt electrodes (5-nm-thick Cr and 80-nm-thick Pt). (12) To pattern the fractal topographical structures of VasES, SU-8/RhBen solution was diluted in cyclopentanone (Sigma-Aldrich) at a 1:2 ratio and patterned by PL by repeating steps 6 and 7. The Si wafer was hard baked at 190–195 °C for 1.5 h. (13) To release probes, the Si wafer was cleaned with oxygen plasma (50 W, 30 s) and then transferred to a Ni etchant solution comprising 40% FeCl₃:39% HCl:H₂O 1:1:20 for 60–120 min. Released probes were rinsed with deionized (DI) water and then transferred to 1× phosphate-buffered saline (PBS) solution (HyClone, GE Healthcare Life Sciences).

Surface functionalization of VasES

The surface of VasES probes was occupied with carboxylic groups after oxygen plasma treatment immediately before the release of probes⁵². The probes were subsequently functionalized through a two-step reaction with 1-ethyl-3-[3-dimethylaminopropyl]carbodiimide/N-hydroxysuccinimide (EDC/NHS) chemistry⁵³. (1) NHS-ester activation. A solution of EDC (ca. 5 mM; Sigma-Aldrich) and NHS (ca. 50 mM; Sigma-Aldrich) in 0.1 M 2-(N-morpholino)ethanesulfonic acid buffered saline (Fisher Scientific) was prepared immediately before the reaction. The probes were loaded into glass capillary tubes (inner diameter 400 µm, outer diameter 650 µm, VWR). The EDC/NHS solution was loaded into the capillary tubes due to capillary action to cover the electrodes, but not the I/O, of the probes. The capillary tubes were left to sit, right side up in the dark. After 1 h, the EDC/NHS solution was drained out of the capillary tubes and rinsed with PBS three times. (2) Laminin coupling. Laminin (Sigma-Aldrich) was diluted in 1× PBS at a 1:9 ratio to a concentration of 100–200 µg ml⁻¹. HiLyte 488-labelled laminin (Cytoskeleton) was used instead, if the probes were to be used for ‘Stability characterization of surface functionalization’. The laminin

solution was loaded into capillary tubes to cover the electrodes, but not the I/O, of the probes. The capillary tubes were left to sit right side up in the dark. After 1 h, the laminin solution was drained out of the capillary tubes and rinsed with 50 mM Tris buffer (pH ca. 7, Sigma-Aldrich) three times to terminate the coupling reaction. The probes were ejected into Tris buffer in glass vials and left to sit at 4 °C until surgery, which was typically 2–12 h later.

Stability characterization of surface functionalization

The surface-functionalized VasES probes were incubated in cell culture medium (BrainBits) in an incubator (Forma Steri-Cult, Thermo Scientific) at 37 °C. The probes were retrieved after 1, 3, 7 and 14 days for fluorescence imaging, after which they were returned to the incubator. The probes were rinsed with DI water and unfolded onto glass slides for fluorescence imaging. Fluorescence images of surface functionalized and control VasES probes across different days (Supplementary Fig. 2) were acquired using the same parameters using a Zeiss LSM 880 confocal/multiphoton microscope (Carl Zeiss Microscopy).

Vertebrate animal subjects

Adult (6–8 weeks, 25–35 g) male C57BL/6J mice (stock no. 000664; The Jackson Laboratory) were used in the study. Exclusion criteria were pre-established: animals with substantial acute implantation damage (>50 µl of initial liquid injection volume) or damage of a major blood vessel were discarded from further experiments.

All procedures were approved by the Animal Care and Use Committee of Harvard University¹⁷ and the Administrative Panel on Laboratory Animal Care of Stanford University. The animal care and use programs at Harvard University and Stanford University meet the requirements of the Federal Law (89–544 and 91–579) and National Institutes of Health regulations and are also accredited by the American Association for Accreditation of Laboratory Animal Care. Before the surgical procedures, animals were group housed on a 12 h:12 h light:dark schedule and fed with food and water ad libitum as appropriate. Animals were housed individually after surgical procedures.

In vivo mouse survival surgery

Step-by-step illustrations are shown in Extended Data Fig. 1.

Cortical resection. The surgical procedure was adapted from glioma resection models⁵⁴. All metal tools in direct contact with the animal subjects were bead sterilized (Fine Science Tools) for 1 h before use, and all plastic tools in direct contact with the animal subjects were sterilized with 70% ethanol and rinsed with sterile DI water and sterile 1× PBS before use. Mice were anaesthetized by intraperitoneal injection of a mixture of 75 mg kg⁻¹ (body weight) of ketamine (Patterson Veterinary Supply) and 1 mg kg⁻¹ dexdomitor (Orion). The degree of anaesthesia was verified via toe pinch before the surgery started. A homeothermic blanket (Harvard Apparatus) was set to 37 °C and placed underneath the anaesthetized mouse. The anaesthetized mouse was placed in a stereotaxic frame (Lab Standard Stereotaxic Instrument, Stoelting Co.) equipped with two ear bars and one nose clamp. Puralube vet ointment (Dechra Pharmaceuticals) was applied on both eyes to moisturize the eye surface throughout the operation. Hair removal lotion (Nair, Church & Dwight) was applied to the scalp for depilation, and Betadine surgical scrub (Purdue Products) was applied to sterilize the depilated scalp skin. A sterile scalpel was used to make a 10 mm longitudinal incision in the scalp along the sagittal sinus. The scalp skin was resected to expose a 10 mm × 10 mm portion of the skull. A dental drill (micromotor with on/off pedal 110/220, Grobet) was used to make a 4 mm (mediolateral) × 2 mm (anteroposterior) cranial window centred at the bregma (Extended Data Fig. 1a). The dura was carefully incised and resected using a sterile 27 gauge needle (PrecisionGlide, Becton Dickinson). The dorsal-most layers of the cerebral cortex in both hemispheres were removed with a spatula (World Precision Instruments),

leaving behind a hemispherical resection cavity (2 mm diameter and 1 mm depth in each hemisphere) and intact margins of dura mater in each hemisphere. Surgical spears (Braintree Scientific) were used to absorb the blood completely. The resection cavity was rinsed with sterile 1× PBS multiple times to ensure minimal amount of blood in the cavity (Extended Data Fig. 1b). Matrigel matrix (product number 356237, Corning; used without dilution) was injected into the resection cavity and sat for 10–15 min to solidify (Extended Data Fig. 1c).

Stereotaxic injection of VasES in mouse brains. In vivo injection of VasES probes into live mice was performed using a controlled stereotaxic injection method as described previously⁵⁵. The VasES probes were sterilized with 70% ethanol and rinsed with sterile DI water and sterile 1× PBS before injection, and then loaded into sterile glass capillaries with an inner diameter of 300 µm and an outer diameter of 400 µm (Produstrial). We note that previous studies from our laboratory¹⁷ and elsewhere^{56,57} reported injections into neural tissue using capillary needles, which are widely adopted for delivering biological species to the brain, have minimal immune response. A 1 mm burr hole was drilled posterior to the resection, then a sterile 0–80 set screw (18–8 stainless-steel cup-point set screw, outer diameter 1.52 mm, groove diameter 1.14 mm, length 4.76 mm; McMaster-Carr Supply Company) was inserted to serve as a point of fixation for the head stage. An identical hole was drilled on the opposite side of the midline and a sterile stainless-steel wire was inserted to a depth of ca. 500 µm to serve as the grounding and reference electrode. Metabond cement (Metabond quick luting cement, Parkell) was used to fix the junction between the stainless-steel wire and the skull. The 3D-printed poly-lactic acid head stages were sterilized with 70% ethanol. Two sterile flexible flat cables (FFCs) folded into L shapes were mounted onto a piece of sterile polyethylene terephthalate fixed to the head stage with Metabond cement. FFCs on head stages were treated by oxygen plasma (100 W, 2 min), and DI water was dropped onto FFC leads to maintain surface hydrophilicity. Metabond cement was used to fix the head stage to the skull and mounting screw. Sterile 1× PBS was swabbed on the skull surface to keep it moist throughout the surgery.

VasES was injected into the targeted brain region using the controlled injection method reported previously⁵⁵ (Extended Data Fig. 1d). In brief, the glass capillary loaded with VasES was inserted in the micropipette holder, which was connected to a 5 ml syringe (Becton Dickinson) pre-filled with 1× PBS and mounted on a syringe pump (PHD 2000, Harvard Apparatus). The glass capillary was positioned at the surface of Matrigel matrix and then inserted through the Matrigel matrix, remaining cortex and SVZ according to the following stereotaxic coordinates: anteroposterior, −0.10 mm; mediolateral, 1.10 mm; dorsoventral, 4.50 mm. Controlled injection was carried out by adjusting the volumetric flow rate and the needle retraction velocity such that the upper part of VasES, which was visualized through an eyepiece camera (DCC1240C, Thorlabs), remained stationary in the field of view. The total injection volume is usually 5–50 µl over 4.5 mm length of injection.

Electrical connection of VasES for electrophysiology studies. Electrical connection of the VasES I/O pads to the FFC used a recently described method⁴⁸. In brief, VasES probes were injected such that the electrodes were fully inside the brain and resection while the I/O pads remained in the capillary. The capillary was moved to above the FFC before ejecting the I/O pads from the capillary onto the FFC and aligning the I/O pads with the FFC leads using a glass pipette (Disposable Pasteur Pipets, VWR). Aligned I/O pads were fully dried by surgical spears and fixed in place using epoxy adhesive (Devcon 5 Minute Epoxy Adhesive, ITW Performance Polymers). The interface was covered with Metabond cement.

Craniotomy closure. Upon the completion of VasES implantation, thin layers of 3% agarose (SeaPlaque agarose, Lonza) hydrogel and

silicone adhesive (Low Toxicity Silicone Adhesive, World Precision Instruments) were applied sequentially on top of the craniotomy to cover the dura defect and assure retention of the Matrigel matrix at the defect site. Metabond cement was applied on top of silicone adhesive and the exposed skull to encapsulate the entire surgical site (Extended Data Fig. 1e).

Post-operative care. After surgery, each mouse was returned to a cage equipped with a 37 °C heating pad. The activity of the mouse was monitored every hour until it was fully recovered from anaesthesia. Buprenex (Buprenorphine, Patterson Veterinary Supply) analgesia was given intraperitoneally at a dose of 0.05 mg kg⁻¹ body weight every 12 h for up to 72 h post-surgery.

3D mapping of the VasES interfaces with the host brain and the resection

Histology sample preparation. The following procedures were performed according to previous work¹⁷ and are reproduced here for completeness. DyLight 649 *Lycopersicon esculentum* TL (50 µl; Vector Laboratories) was injected retro-orbitally into the mice intended for vasculature labelling ca. 10 min before transcardial perfusion. Mice were anaesthetized with ketamine/dexdomitor and transcardially perfused with ice-cold 40 ml 1× PBS and 40 ml 4% formaldehyde (Electron Microscopy Sciences) at specified times post-injection, followed by decapitation. The scalp skin was removed, and the exposed skull was ground at 10,000 rpm using a high-speed rotary tool (Dremel). Brains with the resection and VasES undisturbed were removed from the cranium and placed in 4% formaldehyde for 24 h and then transferred to 1× PBS for another 24 h to remove the remaining formaldehyde. The brains were then embedded in 3% agarose hydrogel, cut into blocks of 2 cm (length) × 2 cm (width) × 1 cm (height). Another VasES probe was injected into the agarose hydrogel block to serve as a reference for the measurement of distance in the subsequent micro-computed tomography and vibratome sectioning steps. In brief, the hydrogel block containing the mouse brain was imaged by a micro-computed tomography X-ray scanning system (HMX ST 225, Nikon Metrology). CT Pro 3D software (Nikon Metrology) was used to calibrate centres of rotation and to reconstruct the images. VGStudio MAX 3.0 software (Volume Graphics) was used to render and analyse the 3D reconstructed images. Distances between the reference VasES and target VasES was measured from reconstructed images. The hydrogel block was cut using a homemade sectioning stage. Finally, a mouse brain was sectioned into 200–800 µm slices using a vibratome (VT1000 S vibrating blade microtome, Leica). The reference VasES was used as a landmark to indicate the distance to the target VasES to facilitate accurate sectioning.

Tissue clearing and immunostaining. Mouse brain slices thicker than ca. 400 µm were cleared using procedures as described previously¹⁷. In brief, brain slices were placed in 1× PBS containing 4% (wt/vol) acrylamide (Sigma-Aldrich) and 0.25% (wt/vol) VA-044 thermal polymerization initiator (Fisher Scientific) at 4 °C for 3 days. The solution was replaced with fresh solution immediately before placing the brain slices in X-CLARITY polymerization system (Logos Biosystems) at 37 °C for 3 h. After polymerization, the brain slices were rinsed with PBST (1× PBS with 0.2% Triton X-100, Thermo Fisher Scientific) before placing them in electrophoretic tissue clearing solution (Logos Biosystems) at 37 °C for 3–5 days until translucent. The brain slices were rinsed once with PBST containing 0.3 M glycine (Sigma-Aldrich), placed in fresh PBST containing 0.3 M glycine and incubated at 4 °C overnight. The brain slices were then placed in fresh PBST and gently shaken for 5 h, with the PBST replaced by fresh solution every hour. The brain slices were incubated with 1:100–1:200 primary antibodies, rabbit anti-DCX (Abcam) or rabbit anti-NeuN (Abcam), and/or rat anti-GFAP (Thermo Fisher Scientific) and/or mouse anti-neurofilament marker

(BioLegend) in PBST at 4 °C for 4 days. After incubation, the brain slices were placed in fresh PBST at 4 °C to let excess antibody diffuse out. The PBST was replaced with fresh solution every 8 h over 2 days. Then, the brain slices were incubated with 1:100–1:200 secondary antibodies, donkey anti-rabbit Alexa Fluor 488 (Abcam) or donkey anti-rabbit Alexa Fluor 647 (Abcam), and/or donkey anti-rat Alexa Fluor 647 (Abcam) and/or donkey anti-mouse Alexa Fluor 594 (Abcam) in PBST at 4 °C for 4 days. The brain slices were placed in fresh PBST containing 1 µg ml⁻¹ 4',6-diamidino-2-phenylindole (DAPI) (Sigma-Aldrich) at 4 °C to let excess antibody diffuse out of the tissue and simultaneously stain nuclear DNA. The PBST with DAPI was replaced with fresh solution every 8 h over 2 days.

For mouse brain slices thinner than ca. 400 µm, tissue clearing was skipped over as diffusion of antibodies without tissue clearing could be achieved in a reasonable time. After vibratome sectioning, brain slices were rinsed once with PBST containing 0.3 M glycine, placed in fresh PBST containing 0.3 M glycine and incubated at 4 °C overnight. The brain slices were then placed in fresh PBST and gently shaken for 5 h, with the PBST replaced by fresh solution every hour. The brain slices were incubated with 1:100–1:200 primary antibodies in PBST at 4 °C for 2 days. After incubation, the brain slices were placed in fresh PBST at 4 °C to let excess antibody diffuse out. The PBST was replaced with fresh solution every 2 h over the course of 12 h. Then, the brain slices were incubated with 1:100–1:200 secondary antibodies in PBST containing 1 µg ml⁻¹ DAPI at 4 °C for 2 days. The brain slices were placed in fresh PBST at 4 °C to let excess antibody diffuse out of the tissue. The PBST was replaced with fresh solution every hour over 6 h.

Refractive index matching. Brain slices were glued at their edge to the bottom of 50-mm-diameter Petri dishes by epoxy adhesive and then incubated in refractive index matching solution PROTOS³⁸ (diatrizoic acid, Sigma-Aldrich; N-methyl-D-glucamine, Sigma-Aldrich; OptiPrep, Accurate Chemical and Scientific) or 80% glycerol:20% PBS (glycerol, Sigma-Aldrich) 24 h before microscopy imaging.

Microscopy imaging. Fluorescence images were acquired on a Zeiss LSM 880 confocal/multiphoton microscope with a 20× objective (numerical aperture 1.0, free working distance 5.6 mm) as previously described¹⁷ or a Leica Stellaris 5 confocal microscope. Confocal images of brain slices were acquired using 405 nm, 488 nm, 561 nm and/or 633 nm lasers as the excitation sources for DAPI, Alexa Fluor 488, RhBEN and/or Alexa Fluor 647/DyLight 649, respectively. Images were acquired by taking tile scan together with Zstacks, with a voxel size of 0.2–1.0 µm (X) × 0.2–1.0 µm (Y) × 1.0–2.5 µm (Z) and tile scan overlap of 10%. Image data analysis is detailed in Supplementary Note 3.

Electrophysiological recording

The following procedures were performed according to previous work¹⁷ and are reproduced here for completeness. The electrophysiology of awake and restrained mice was recorded for ca. 30 min twice a week. Head-mounted FFCs of mice were connected to an Intan RHD recording controller (Intan Technologies) through a homemade printed circuit board while mice were restrained in a Tailveiner restrainer (Braintree Scientific). The stainless-steel wire was used as a reference. Electrophysiological recordings were acquired with a 20 kHz sampling rate and a 60 Hz notch filter. The electrical impedance of each recording electrode at 1 kHz was also measured and showed consistent values of <1 MΩ that allow for single-unit recording measurements (Supplementary Fig. 6). The analysis of electrophysiological data is detailed in Supplementary Note 2.

Rotarod test

Motor coordination in mice before and after surgery was assessed using the rotarod test⁴¹. Mice were placed on a rotating rod (Harvard

Apparatus) that steadily accelerated from 4 to 40 rpm over 2 min, and the latency to fall was recorded. Statistical methods can be found in Supplementary Note 4.

Reporting summary

Further information on research design is available in the Nature Portfolio Reporting Summary linked to this article.

Data availability

The data supporting the results in this study are available within the paper and its Supplementary Information. Source data are available in the Harvard Dataverse with the identifier <https://doi.org/10.7910/DVN/4HIWCA>.

Code availability

The custom code used in this study is available at https://github.com/XiaoYangPhD/Yang_2023_NBME.

References

- Barker, R. A., Götz, M. & Parmar, M. New approaches for brain repair—from rescue to reprogramming. *Nature* **557**, 329–334 (2018).
- Martino, G. & Pluchino, S. The therapeutic potential of neural stem cells. *Nat. Rev. Neurosci.* **7**, 395–406 (2006).
- Carlson, A. L. et al. Generation and transplantation of reprogrammed human neurons in the brain using 3D microtopographic scaffolds. *Nat. Commun.* **7**, 10862 (2016).
- Nih, L. R., Gojgini, S., Carmichael, S. T. & Segura, T. Dual-function injectable angiogenic biomaterial for the repair of brain tissue following stroke. *Nat. Mater.* **17**, 642–651 (2018).
- Falkner, S. et al. Transplanted embryonic neurons integrate into adult neocortical circuits. *Nature* **539**, 248–253 (2016).
- Trounson, A. & McDonald, C. Stem cell therapies in clinical trials: progress and challenges. *Cell Stem Cell* **17**, 11–22 (2015).
- Green, J. J. & Elisseeff, J. H. Mimicking biological functionality with polymers for biomedical applications. *Nature* **540**, 386–394 (2016).
- Hussey, G. S., Dziki, J. L. & Badylak, S. F. Extracellular matrix-based materials for regenerative medicine. *Nat. Rev. Mater.* **3**, 159–173 (2018).
- Koffler, J. et al. Biomimetic 3D-printed scaffolds for spinal cord injury repair. *Nat. Med.* **25**, 263–269 (2019).
- Feiner, R. & Dvir, T. Tissue–electronics interfaces: from implantable devices to engineered tissues. *Nat. Rev. Mater.* **3**, 17076 (2017).
- Frank, J. A., Antonini, M.-J. & Anikeeva, P. Next-generation interfaces for studying neural function. *Nat. Biotechnol.* **37**, 1013–1023 (2019).
- Chen, X., Rogers, J. A., Lacour, S. P., Hu, W. & Kim, D.-H. Materials chemistry in flexible electronics. *Chem. Soc. Rev.* **48**, 1431–1433 (2019).
- Luan, L. et al. Recent advances in electrical neural interface engineering: minimal invasiveness, longevity, and scalability. *Neuron* **108**, 302–321 (2020).
- Tian, B. Z. et al. Macroporous nanowire nanoelectronic scaffolds for synthetic tissues. *Nat. Mater.* **11**, 986–994 (2012).
- Kalmykov, A. et al. Organ-on-a-chip: three-dimensional self-rolled biosensor array for electrical interrogations of human electrogenic spheroids. *Sci. Adv.* **5**, eaax0729 (2019).
- Floch, P. L. et al. Stretchable mesh nanoelectronics for three-dimensional single-cell chronic electrophysiology from developing brain organoids. *Adv. Mater.* **34**, 2106829 (2022).
- Yang, X. et al. Bioinspired neuron-like electronics. *Nat. Mater.* **18**, 510–517 (2019).
- Wang, L. et al. Functionalized helical fibre bundles of carbon nanotubes as electrochemical sensors for long-term in vivo monitoring of multiple disease biomarkers. *Nat. Biomed. Eng.* **4**, 159–171 (2020).
- Woodington, B. J. et al. Electronics with shape actuation for minimally invasive spinal cord stimulation. *Sci. Adv.* **7**, eabg7833 (2021).
- Chen, J. C. et al. A wireless millimetric magnetoelectric implant for the endovascular stimulation of peripheral nerves. *Nat. Biomed. Eng.* **6**, 706–716 (2022).
- Zhao, Z. et al. Ultraflexible electrode arrays for months-long high-density electrophysiological mapping of thousands of neurons in rodents. *Nat. Biomed. Eng.* **7**, 520–532 (2023).
- Goldman, S. A. & Chen, Z. Perivascular instruction of cell genesis and fate in the adult brain. *Nat. Neurosci.* **14**, 1382–1389 (2011).
- Ming, G.-L. & Song, H. Adult neurogenesis in the mammalian brain: significant answers and significant questions. *Neuron* **70**, 687–702 (2011).
- Fujioka, T. et al. β 1 integrin signaling promotes neuronal migration along vascular scaffolds in the post-stroke brain. *EBioMedicine* **16**, 195–203 (2017).
- Todorov, M. I. et al. Machine learning analysis of whole mouse brain vasculature. *Nat. Methods* **17**, 442–449 (2020).
- Jeffries, E. M. & Wang, Y. Incorporation of parallel electrospun fibers for improved topographical guidance in 3D nerve guides. *Biofabrication* **5**, 035015 (2013).
- Wei, H., George, C. M. & Ravi, V. B. Nanoscale laminin coating modulates cortical scarring response around implanted silicon microelectrode arrays. *J. Neural Eng.* **3**, 316 (2006).
- Aisenbrey, E. A. & Murphy, W. L. Synthetic alternatives to Matrigel. *Nat. Rev. Mater.* **5**, 539–551 (2020).
- Magavi, S. S., Leavitt, B. R. & Macklis, J. D. Induction of neurogenesis in the neocortex of adult mice. *Nature* **405**, 951–955 (2000).
- Zhao, C., Deng, W. & Gage, F. H. Mechanisms and functional implications of adult neurogenesis. *Cell* **132**, 645–660 (2008).
- Sultan, S. et al. Synaptic integration of adult-born hippocampal neurons is locally controlled by astrocytes. *Neuron* **88**, 957–972 (2015).
- Wellman, S. M., Li, L., Yaxiaer, Y., McNamara, I. & Kozai, T. D. Y. Revealing spatial and temporal patterns of cell death, glial proliferation, and blood–brain barrier dysfunction around implanted intracortical neural interfaces. *Front. Neurosci.* **13**, 493 (2019).
- Villacampa, N., Almolda, B., González, B. & Castellano, B. in *Microglia: Methods and Protocols* (eds Joseph, B. & Venero, J. L.) 261–279 (Humana, 2013).
- Lledo, P.-M., Alonso, M. & Grubb, M. S. Adult neurogenesis and functional plasticity in neuronal circuits. *Nat. Rev. Neurosci.* **7**, 179–193 (2006).
- Lerner, T. N., Ye, L. & Deisseroth, K. Communication in neural circuits: tools, opportunities, and challenges. *Cell* **164**, 1136–1150 (2016).
- Lindvall, O. & Kokaia, Z. Neurogenesis following stroke affecting the adult brain. *Cold Spring Harb. Perspect. Biol.* **7**, a019034 (2015).
- Kumar, A., Rotter, S. & Aertsen, A. Spiking activity propagation in neuronal networks: reconciling different perspectives on neural coding. *Nat. Rev. Neurosci.* **11**, 615–627 (2010).
- Khodagholy, D. et al. NeuroGrid: recording action potentials from the surface of the brain. *Nat. Neurosci.* **18**, 310–315 (2015).
- Barthó, P. et al. Characterization of neocortical principal cells and interneurons by network interactions and extracellular features. *J. Neurophysiol.* **92**, 600–608 (2004).
- Denoth-Lippuner, A. & Jessberger, S. Formation and integration of new neurons in the adult hippocampus. *Nat. Rev. Neurosci.* **22**, 223–236 (2021).
- Hua, Y. et al. Peripheral SMN restoration is essential for long-term rescue of a severe spinal muscular atrophy mouse model. *Nature* **478**, 123–126 (2011).

42. Lichtman, J. W., Livet, J. & Sanes, J. R. A technicolour approach to the connectome. *Nat. Rev. Neurosci.* **9**, 417–422 (2008).
43. Werner, C., Sauer, M. & Geis, C. Super-resolving microscopy in neuroscience. *Chem. Rev.* **121**, 11971–12015 (2021).
44. Oh, S. W. et al. A mesoscale connectome of the mouse brain. *Nature* **508**, 207 (2014).
45. Glover, G. H. Overview of functional magnetic resonance imaging. *Neurosurg. Clin. N. Am.* **22**, 133–139 (2011).
46. Fu, T.-M. et al. Stable long-term chronic brain mapping at the single-neuron level. *Nat. Methods* **13**, 875–882 (2016).
47. Grefkes, C. & Fink, G. R. Recovery from stroke: current concepts and future perspectives. *Neurol. Res. Pract.* **2**, 17 (2020).
48. Lee, J. M. et al. Nanoenabled direct contact interfacing of syringe-injectable mesh electronics. *Nano Lett.* **19**, 5818–5826 (2019).
49. Lee, J. M. et al. Scalable three-dimensional recording electrodes for probing biological tissues. *Nano Lett.* **22**, 4552–4559 (2022).
50. Fu, T.-M., Hong, G., Viveros, R. D., Zhou, T. & Lieber, C. M. Highly scalable multichannel mesh electronics for stable chronic brain electrophysiology. *Proc. Natl Acad. Sci. USA* **114**, E10046–E10055 (2017).
51. Jun, J. J. et al. Fully integrated silicon probes for high-density recording of neural activity. *Nature* **551**, 232–236 (2017).
52. Ferdinand, W. et al. Stability of the hydrophilic behavior of oxygen plasma activated SU-8. *J. Micromech. Microeng.* **17**, 524–531 (2007).
53. Fischer, M. J. E. *Surface Plasmon Resonance: Methods and Protocols* (Humana, 2010).
54. Bastiancich, C., Danhier, P., Préat, V. & Danhier, F. Anticancer drug-loaded hydrogels as drug delivery systems for the local treatment of glioblastoma. *J. Control. Release* **243**, 29–42 (2016).
55. Hong, G. S. et al. Syringe injectable electronics: precise targeted delivery with quantitative input/output connectivity. *Nano Lett.* **15**, 6979–6984 (2015).
56. Reza, M. et al. In vivo migration of endogenous brain progenitor cells guided by an injectable peptide amphiphile biomaterial. *J. Tissue Eng. Regen. Med.* **12**, e2123–e2133 (2018).
57. Peden, C. S. et al. Striatal readministration of rAAV vectors reveals an immune response against AAV2 capsids that can be circumvented. *Mol. Ther.* **17**, 524–537 (2009).
58. Murray, E. et al. Simple, scalable proteomic imaging for high-dimensional profiling of intact systems. *Cell* **163**, 1500–1514 (2015).

Acknowledgements

The authors gratefully acknowledge S. Badylak, M. Murdock and Y.v.d. Merwe, who provided useful discussions and crucial insights for the generation and evaluation of the brain resection model at the initial stage of this work. We thank the assistance from J. Lee for the cross-correlation analysis, A. Zhang for the functionalization-stability characterization, T. Gao for electrophysiology recording instrumentation and T.-M. Fu for helpful discussions during the initial stages of this work. We thank Z. Ou, S. Zhao, X. Wu, G. Woods, and J. Shadrach for assistance with animal surgeries and vibratome sectioning. C.M.L. discloses support for the research described in this

study from the National Institute on Drug Abuse (1R21DA043985-01) and the Director's Pioneer Award (1DP1EB025835-01) of the National Institutes of Health. N.J.R. discloses support from a Stanford Bio-X Honorary Graduate Student Fellowship and the National Science Foundation Graduate Research Fellowship Program (DGE-1656518). This work was performed in part at the Harvard Center for Biological Imaging and Harvard University Center for Nanoscale Systems, a member of the National Nanotechnology Coordinated Infrastructure Network supported by the National Science Foundation.

Author contributions

X.Y. and C.M.L. designed the experiments. X.Y. performed experiments including device fabrication, surface functionalization, animal surgeries, histology and electrophysiology. Y.Q. performed experiments including device fabrication, surface functionalization and histology at Harvard University. C.W. contributed to schematic illustrations and figure designs. T.J.Z. helped establish the surface functionalization and histology protocols. N.J.R. performed the finite-element simulations. G.H. helped establish the system and provided feedback. X.Y., Y.Q., C.W. and C.M.L. analysed the data. X.Y. and C.M.L. wrote the paper. All authors discussed the results, revised or commented on the manuscript.

Competing interests

The authors declare no competing interests.

Additional information

Extended data is available for this paper at <https://doi.org/10.1038/s41551-023-01101-6>.

Supplementary information The online version contains supplementary material available at <https://doi.org/10.1038/s41551-023-01101-6>.

Correspondence and requests for materials should be addressed to Xiao Yang, Guosong Hong or Charles M. Lieber.

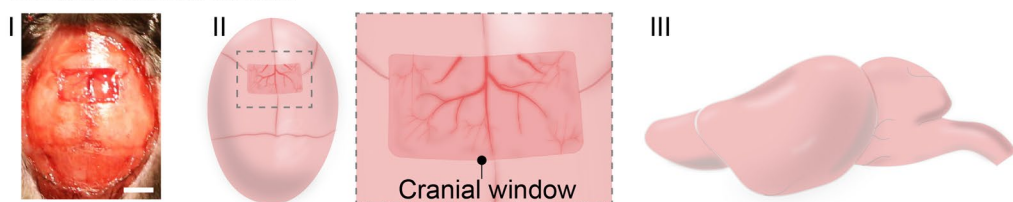
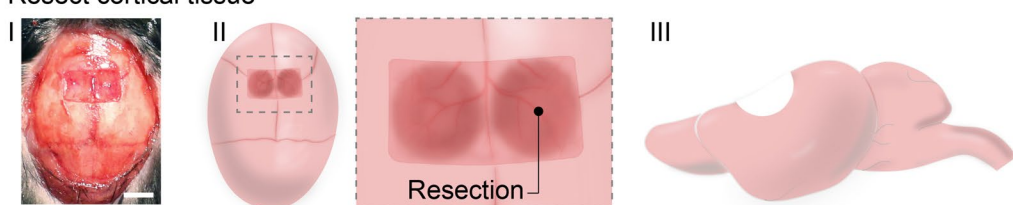
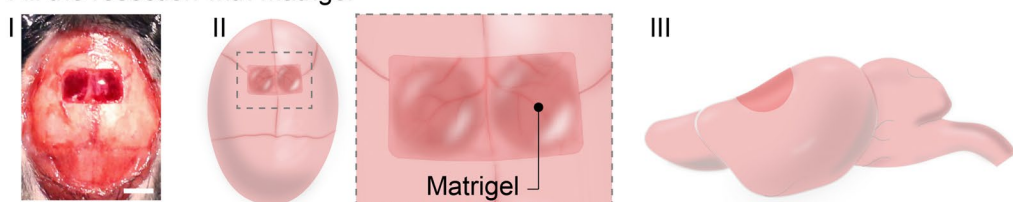
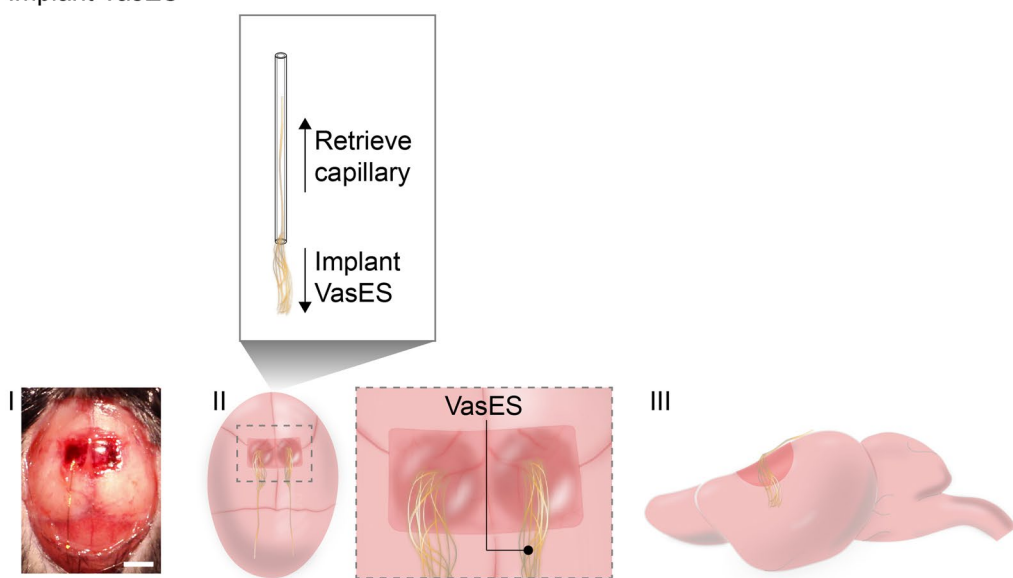
Peer review information *Nature Biomedical Engineering* thanks Eric Glowacki, Jacob Robinson, Darren Svirskis and the other, anonymous, reviewer(s) for their contribution to the peer review of this work. Peer reviewer reports are available.

Reprints and permissions information is available at www.nature.com/reprints.

Publisher's note Springer Nature remains neutral with regard to jurisdictional claims in published maps and institutional affiliations.

Springer Nature or its licensor (e.g. a society or other partner) holds exclusive rights to this article under a publishing agreement with the author(s) or other rightsholder(s); author self-archiving of the accepted manuscript version of this article is solely governed by the terms of such publishing agreement and applicable law.

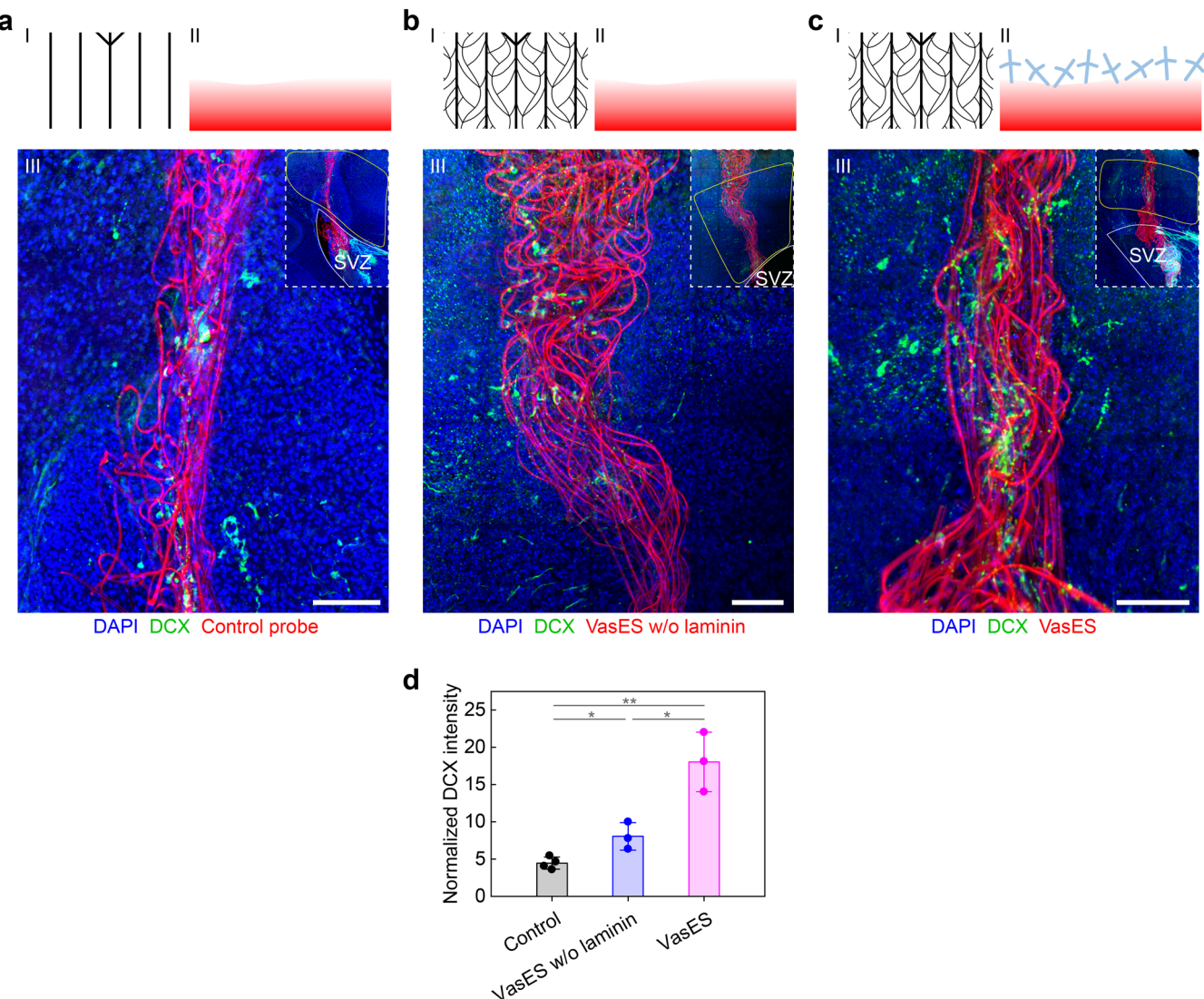
© The Author(s), under exclusive licence to Springer Nature Limited 2023

a Generate cranial window**b Resect cortical tissue****c Fill the resection with Matrigel****d Implant VasES****e Seal cranial window**

Extended Data Fig. 1 | See next page for caption.

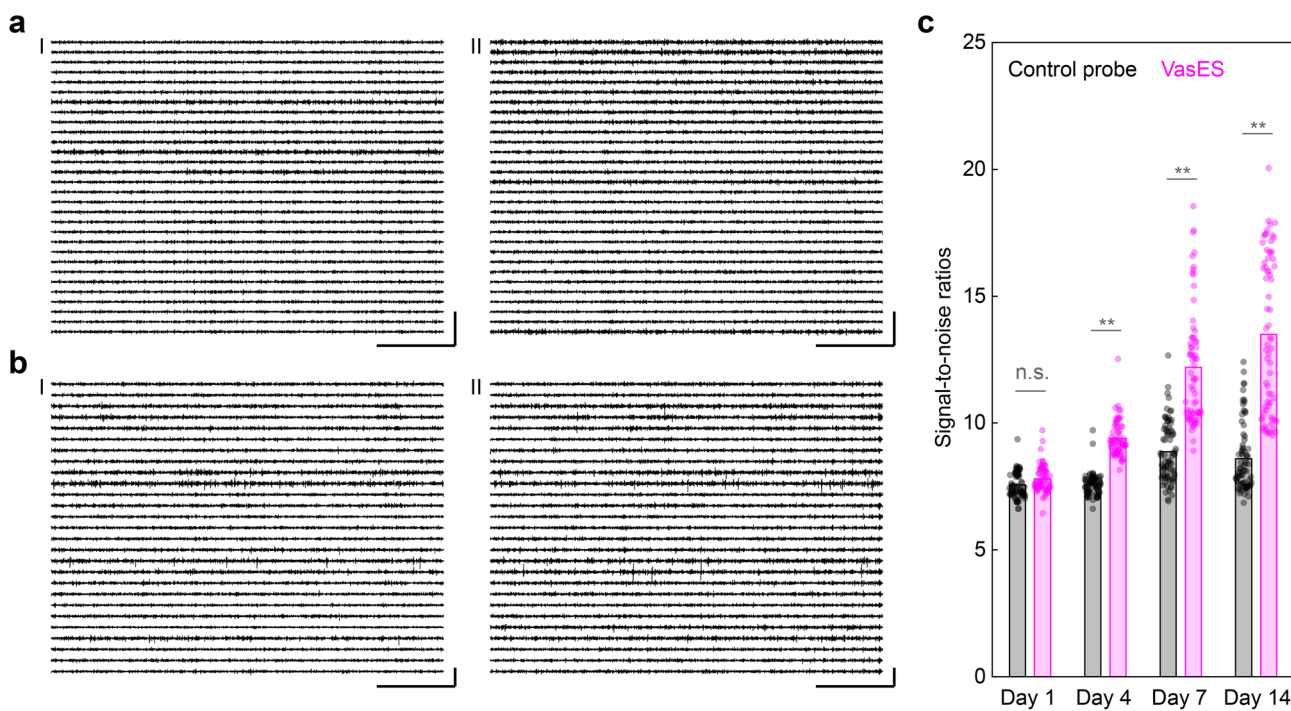
Extended Data Fig. 1 | Photographs and schematics illustrating the processes of brain resection surgery and VasES implantation. In each panel, **I**, **II** and **III** show photographs, top view schematics and side view schematics, respectively. **a**, Generate a cranial window centered at bregma with a lateral dimension of 4 mm (mediolateral) by 2 mm (anteroposterior). **b**, Resect cortical tissue to the depth of 1 mm in each hemisphere, leaving behind the resection cavity and intact

margins of dura. **c**, Fill the resection with Matrigel and let it sit for 10–15 min to solidify. **d**, Stereotactically implant VasES throughout the cortical resection, remaining cortical tissue and SVZ. Bond the input-output interface of electronics to flat flexible cable for electrophysiology recording. **e**, Seal the cranial window with agarose, silicone adhesive and dental cement sequentially. Scale bars, 2 mm.



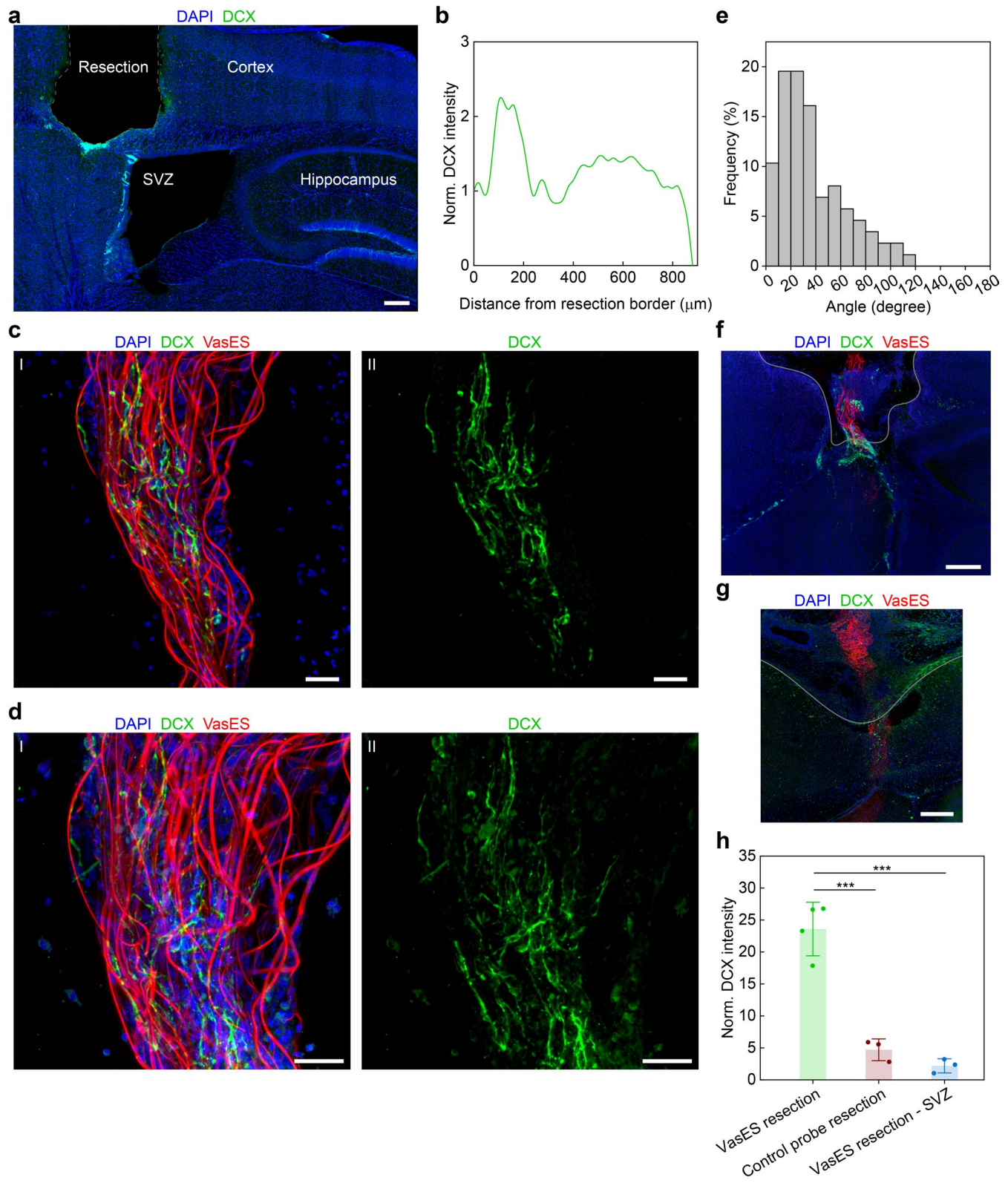
Extended Data Fig. 2 | Efficacy of VasES in directing the migration of SVZ newborn neurons by histology assessment. **a, b, and c** represent control probe, VasES without laminin, and VasES, respectively. **I, II** and **III** show topographical design, surface functionalization and fluorescence images, respectively, at 1 week post-implantation. The insets feature larger area images, with the SVZ and the volumes used for quantification of DCX intensity outlined with white and yellow contours, respectively. Scale bars, 100 μm . **d**, Comparison

of normalized DCX fluorescence intensity within 60 μm from control probes ($N=4$), VasES without laminin functionalization ($N=3$), and VasES with laminin functionalization ($N=3$) at 1 week post-injection (details in the Supplementary Note 3). Independent samples were collected from different mice for each group. Error bars represent ± 1 s.d. $^{**}P=1.02 \times 10^{-3}$ (control versus VasES), $^*P=1.61 \times 10^{-2}$ (control versus VasES without laminin), $^*P=1.70 \times 10^{-2}$ (VasES without laminin versus VasES); two-tailed *t*-test.


Extended Data Fig. 3 | Evaluation of VasES by electrophysiology recording.

Representative multiplexed electrophysiology recordings of control probe (a) and VasES (b) at 7 (I) and 14 (II) days post-implantation. Scale bars, 100 ms (lateral) and 100 μ V (vertical). c, Bar chart of chronic electrophysiology recording signal-to-noise ratios (SNRs) of control probe and VasES (details in the

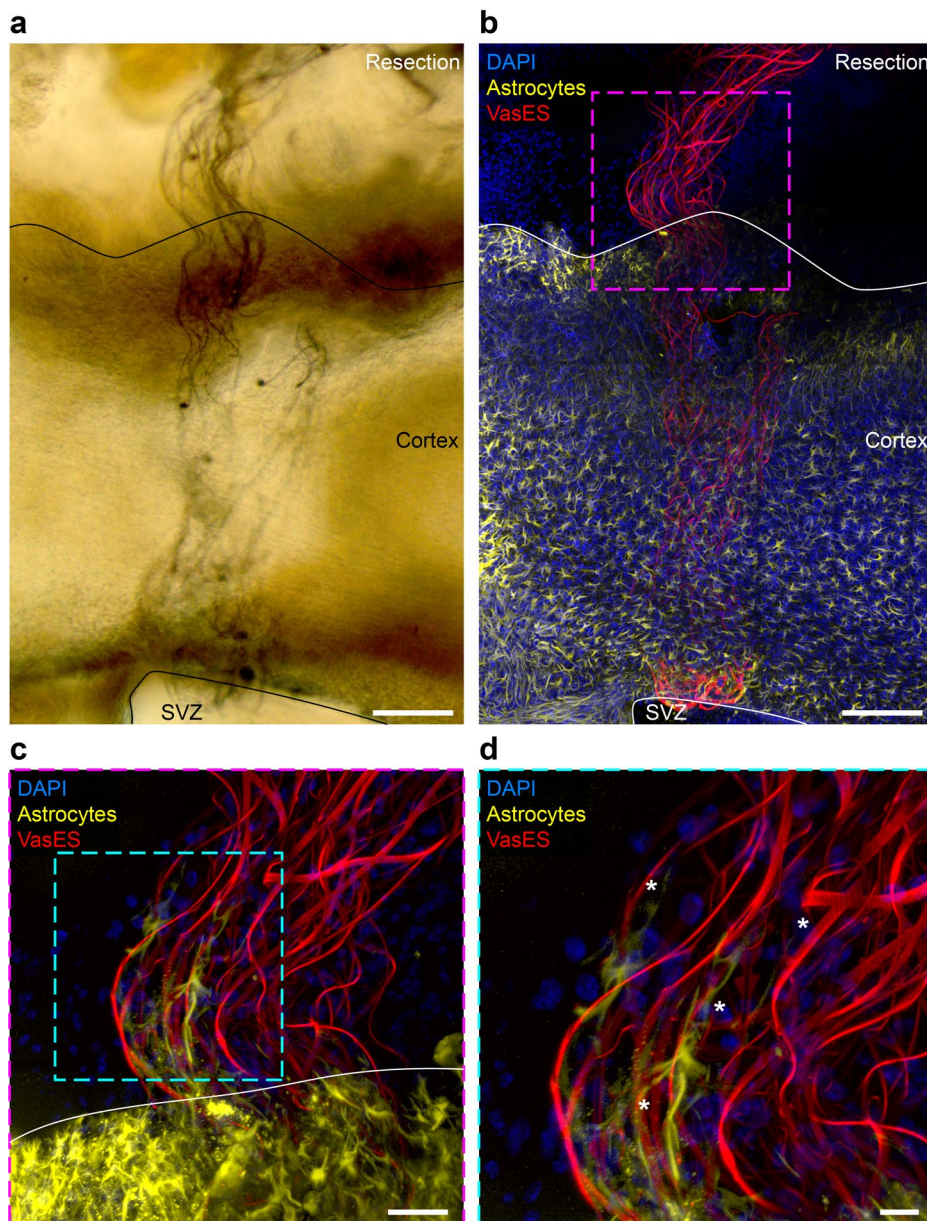
Supplementary Note 2), showing that VasES has higher SNRs than control probe on 4–14 days post-implantation. Data includes 77 channels from 3 control probes and 69 channels from 3 VasES probes. Left to right, $P = 0.316$, ** $P = 1.63 \times 10^{-3}$, ** $P = 8.28 \times 10^{-3}$, ** $P = 4.51 \times 10^{-3}$; two-tailed t -test. Bars represent mean values.



Extended Data Fig. 4 | See next page for caption.

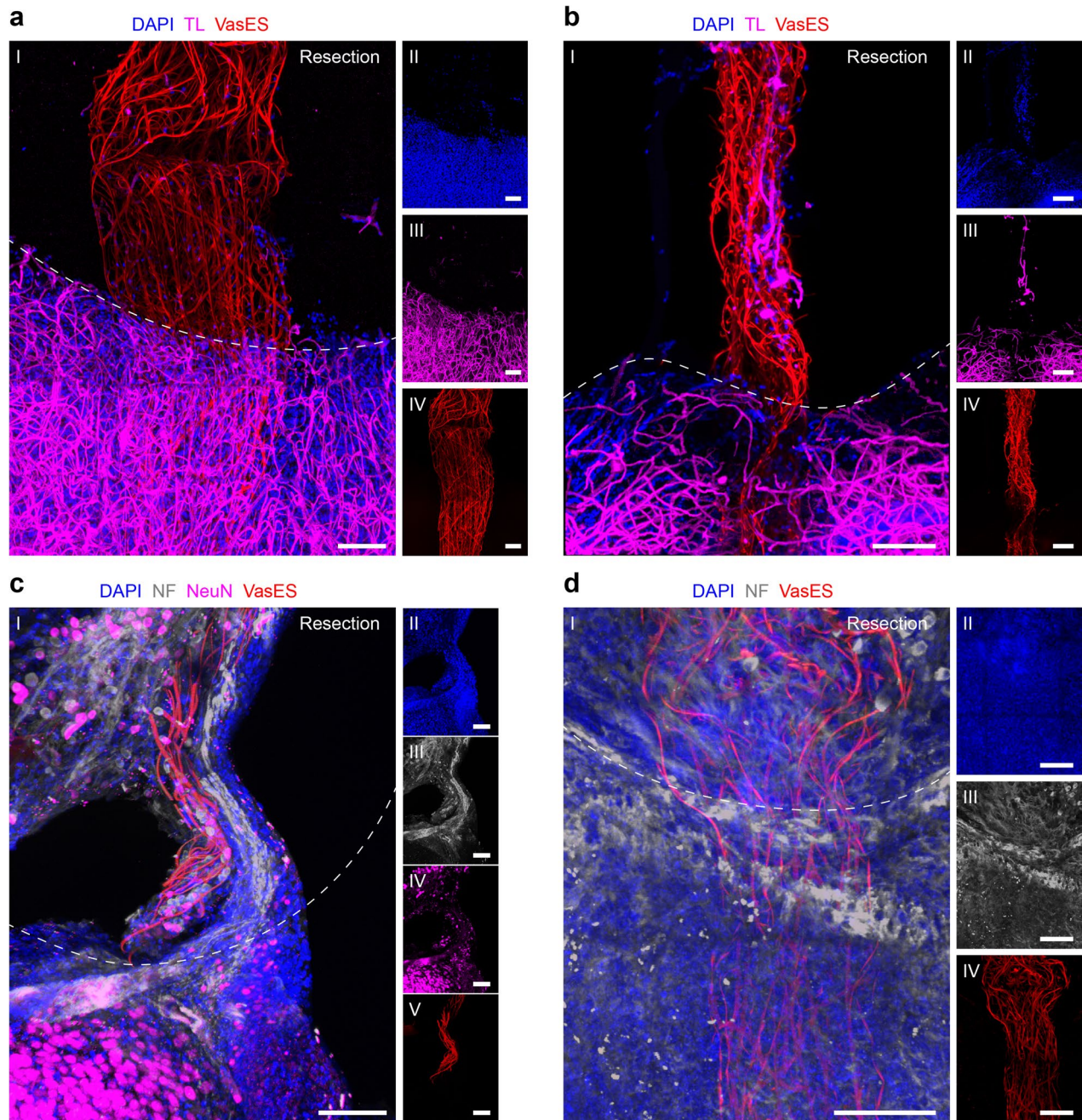
Extended Data Fig. 4 | Histology characterization of migration of newborn neurons. **a**, An overview fluorescence image of control brain resection of which Fig. 2a is derived from, showing the relative position of the cortical resection with respect to SVZ. Scale bar, 200 μm . **b**, DCX fluorescence intensity profile along VasES in the resection as a function of the distance from the resection boundary (normalized against the intensity at the resection border; details in the Supplementary Note 3). **c**, Fluorescence image shown in Fig. 2c is displayed at a larger scale (**I**) and the corresponding DCX channel of the same image (**II**). The DCX data shows that the leading processes of the newborn neurons are closely associated and aligned with the VasES structural elements. **d**, Close-up fluorescence image captured at a higher resolution on the sample shown in Fig. 2c, showing the characteristic DCX morphology. **e**, Distribution of angle between leading processes of DCX⁺ newborn neurons and VasES structures ($N=87$). **f**, Fluorescence image of implantation of control probe into the

resection at 1 week post-implantation. The gray curve delineates the resection boundary. **g**, Fluorescence image of VasES implantation into cortical resection without insertion into the SVZ at 1 week post-implantation. The gray curve delineates the resection boundary. **h**, Quantitative analysis of normalized DCX fluorescence intensity at 0–60 μm near control probes ($N=3$ independent samples; ‘control probe resection’) and near VasES without insertion into the SVZ ($N=3$ independent samples; ‘VasES resection - SVZ’) at 1 week post-implantation (details in the Supplementary Note 3). The quantification of VasES implantation in the resection (‘VasES resection’), as presented in Fig. 2e, is also replicated here for comparison. *** $P=7.84\times10^{-4}$ (VasES resection versus control probe resection), *** $P=3.80\times10^{-4}$ (VasES resection versus VasES resection - SVZ), two-tailed *t*-test. Error bars reflect ± 1 s.d. Scale bars, 50 μm for **c** and **d**, 300 μm for **f** and **g**.



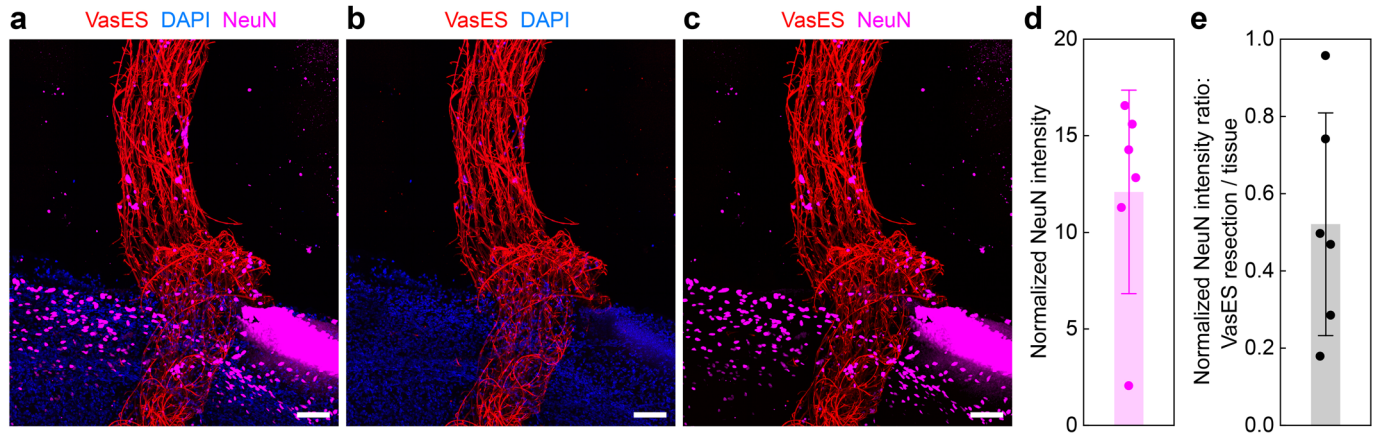
Extended Data Fig. 5 | Migration of astrocytes along VasES into cortical resection. Optical microscope image (a) and fluorescence image (b) of the same field of view of VasES-implanted tissue at 1 week post-implantation. c, Zoomed-in image of the magenta dashed box in b, showing the migration of astrocytes into

the resection. d, Close-up image of the cyan dashed box in c. The white asterisks highlight the alignment of migrating astrocytes with VasES elements. The black and white curves delineate the resection boundary. Scale bars, 200 μm for a and b, 50 μm for c, 20 μm for d.



Extended Data Fig 6 | Histology characterization of tomato lectin⁺ cells and neurofilaments. **a** and **b**, Infiltration of tomato lectin (TL)-positive endothelial cells and microglia into the cortical resection at 1 week (**a**) and 2 weeks (**b**) post-

implantation. **c** and **d**, Infiltration of neurofilaments into the cortical resection at 4 weeks (**c**) and 3 months (**d**) post-implantation. The white dashed curves delineate the resection boundary. Scale bars, 100 μ m.



Extended Data Fig 7 | Histology characterization of NeuN⁺ neuronal nuclei in the cortical resection. **a–c**, Fluorescence images showing the development of newborn neurons at 4 weeks post-implantation. Scale bars, 100 μm . Colocalization quantification shows that 99.0% of NeuN⁺ cells in cortical resection are DAPI⁺, demonstrating that the NeuN immunostaining is highly specific, and that false positive staining is largely excluded. **d**, Quantitative analysis of normalized NeuN fluorescence intensity within 60 μm from VasES elements at 4 weeks post-implantation on $N = 6$ independent samples. Error bar

represents ± 1 s.d. The normalized NeuN intensity is calculated as the ratio of the average fluorescence intensity within 60 μm from VasES versus the baseline value as the average fluorescence intensity 340–400 μm away. **e**, Normalized NeuN intensity along VasES probes in the cortical resection versus NeuN intensity in the undamaged native tissue. This is calculated as the ratio of the average fluorescence intensity along the VasES versus the average fluorescence intensity in the undamaged native tissue. Error bar represents ± 1 s.d.

Reporting Summary

Nature Portfolio wishes to improve the reproducibility of the work that we publish. This form provides structure for consistency and transparency in reporting. For further information on Nature Portfolio policies, see our [Editorial Policies](#) and the [Editorial Policy Checklist](#).

Statistics

For all statistical analyses, confirm that the following items are present in the figure legend, table legend, main text, or Methods section.

n/a Confirmed

- The exact sample size (n) for each experimental group/condition, given as a discrete number and unit of measurement
- A statement on whether measurements were taken from distinct samples or whether the same sample was measured repeatedly
- The statistical test(s) used AND whether they are one- or two-sided
Only common tests should be described solely by name; describe more complex techniques in the Methods section.
- A description of all covariates tested
- A description of any assumptions or corrections, such as tests of normality and adjustment for multiple comparisons
- A full description of the statistical parameters including central tendency (e.g. means) or other basic estimates (e.g. regression coefficient) AND variation (e.g. standard deviation) or associated estimates of uncertainty (e.g. confidence intervals)
- For null hypothesis testing, the test statistic (e.g. F , t , r) with confidence intervals, effect sizes, degrees of freedom and P value noted
Give P values as exact values whenever suitable.
- For Bayesian analysis, information on the choice of priors and Markov chain Monte Carlo settings
- For hierarchical and complex designs, identification of the appropriate level for tests and full reporting of outcomes
- Estimates of effect sizes (e.g. Cohen's d , Pearson's r), indicating how they were calculated

Our web collection on [statistics for biologists](#) contains articles on many of the points above.

Software and code

Policy information about [availability of computer code](#)

Data collection	ZEN software and LAS X software were used to acquire the fluorescence images. The Intan system was used to acquire electrophysiology data. No custom software or code were used for data collection.
Data analysis	Imaris (version 9), ImageJ (1.53q) and MATLAB (R2018b and R2019a) were used for data analysis. COMSOL Multiphysics (5.6) was used for finite-element simulation.

For manuscripts utilizing custom algorithms or software that are central to the research but not yet described in published literature, software must be made available to editors and reviewers. We strongly encourage code deposition in a community repository (e.g. GitHub). See the Nature Portfolio [guidelines for submitting code & software](#) for further information.

Data

Policy information about [availability of data](#)

All manuscripts must include a [data availability statement](#). This statement should provide the following information, where applicable:

- Accession codes, unique identifiers, or web links for publicly available datasets
- A description of any restrictions on data availability
- For clinical datasets or third party data, please ensure that the statement adheres to our [policy](#)

The data supporting the results in this study are available within the paper and its Supplementary Information. Source data are available in the Harvard Dataverse with the identifier <https://doi.org/10.7910/DVN/4HIWCA>.

Research involving human participants, their data, or biological material

Policy information about studies with [human participants or human data](#). See also policy information about [sex, gender \(identity/presentation\), and sexual orientation](#) and [race, ethnicity and racism](#).

Reporting on sex and gender

The study did not involve human participants.

Reporting on race, ethnicity, or other socially relevant groupings

—

Population characteristics

—

Recruitment

—

Ethics oversight

—

Note that full information on the approval of the study protocol must also be provided in the manuscript.

Field-specific reporting

Please select the one below that is the best fit for your research. If you are not sure, read the appropriate sections before making your selection.

Life sciences

Behavioural & social sciences

Ecological, evolutionary & environmental sciences

For a reference copy of the document with all sections, see nature.com/documents/nr-reporting-summary-flat.pdf

Life sciences study design

All studies must disclose on these points even when the disclosure is negative.

Sample size

Sample sizes were selected to achieve at least 80% power at a significance level of 0.05.

Data exclusions

Exclusion criteria were pre-established: animals with substantial acute implantation damage (>50 µl of initial liquid injection volume) or with damage of a major blood vessel were discarded from further experiments.

Replication

Replicate experiments on independent animals were performed to ensure the reproducibility of the results. The attempts at replication were successful and the conclusions were drawn from the analysis of multiple experiments.

Randomization

Mice were randomized into different experimental groups.

Blinding

Blinding was used during fluorescence-image analysis.

Reporting for specific materials, systems and methods

We require information from authors about some types of materials, experimental systems and methods used in many studies. Here, indicate whether each material, system or method listed is relevant to your study. If you are not sure if a list item applies to your research, read the appropriate section before selecting a response.

Materials & experimental systems

n/a	Involved in the study
<input type="checkbox"/>	<input checked="" type="checkbox"/> Antibodies
<input checked="" type="checkbox"/>	<input type="checkbox"/> Eukaryotic cell lines
<input checked="" type="checkbox"/>	<input type="checkbox"/> Palaeontology and archaeology
<input type="checkbox"/>	<input checked="" type="checkbox"/> Animals and other organisms
<input checked="" type="checkbox"/>	<input type="checkbox"/> Clinical data
<input checked="" type="checkbox"/>	<input type="checkbox"/> Dual use research of concern
<input type="checkbox"/>	<input checked="" type="checkbox"/> Plants

Methods

n/a	Involved in the study
<input checked="" type="checkbox"/>	<input type="checkbox"/> ChIP-seq
<input checked="" type="checkbox"/>	<input type="checkbox"/> Flow cytometry
<input checked="" type="checkbox"/>	<input type="checkbox"/> MRI-based neuroimaging

Antibodies

Antibodies used

Primary antibodies: rabbit anti-doublecortin (Abcam, ab18723), rabbit anti-NeuN (Abcam, ab177487), rat anti-GFAP (Thermo Fisher Scientific, 13-0300), mouse anti-neurofilament marker (BioLegend, 837904).

Secondary antibodies: donkey anti-rabbit Alexa Fluor 488 (Abcam, ab150073), donkey anti-rabbit Alexa Fluor 647 (Abcam, ab150075), donkey anti-rat Alexa Fluor 647 (Abcam, ab150155), donkey anti-mouse Alexa Fluor 594 (Abcam, ab150108).

Validation

All the primary antibodies used in this study have been validated on mouse brain tissues by the supplier and by customers, as shown on the supplier's website.

Animals and other research organisms

Policy information about [studies involving animals](#); [ARRIVE guidelines](#) recommended for reporting animal research, and [Sex and Gender in Research](#)

Laboratory animals

6–8-weeks-old male C57BL/6J mice (Jackson Laboratory, stock number 000664) were used.

Wild animals

The study did not involve wild animals.

Reporting on sex

Only male mice were used.

Field-collected samples

The study did not involve samples collected from the field.

Ethics oversight

All procedures were approved by the Animal Care and Use Committee of Harvard University and the Administrative Panel on Laboratory Animal Care (APLAC) of Stanford University. The animal care and use programs at Harvard University and Stanford University meet the requirements of the Federal Law (89-544 and 91-579) and NIH regulations, and are also accredited by the American Association for Accreditation of Laboratory Animal Care (AAALAC).

Note that full information on the approval of the study protocol must also be provided in the manuscript.